

THE BLACK HOLE MASS-STELLAR VELOCITY DISPERSION RELATION OF NARROW-LINE SEYFERT 1 GALAXIES

JONG-HAK WOO¹, YOSEP YOON¹, SONGYOUN PARK¹, DAESEONG PARK², AND SANG CHUL KIM³

¹Department of Physics and Astronomy, Seoul National University, Seoul, 151-742, Republic of Korea

²Department of Physics and Astronomy, University of California, Irvine, CA 92697-4575, USA

³Korea Astronomy and Space Science Institute, Daejeon, 305-348 and Korea University of Science and Technology (UST), Daejeon, 305-350, Republic of Korea

Draft version

ABSTRACT

Narrow-line Seyfert 1 galaxies (NLS1s) are arguably one of the key AGN subclasses in investigating the origin of the black hole mass - stellar velocity dispersion ($M_{\text{BH}} - \sigma_*$) relation because of their high accretion rate and significantly low M_{BH} . Currently, it is under discussion whether present-day NLS1s offset from the $M_{\text{BH}} - \sigma_*$ relation. Using the directly measured stellar velocity dispersion of 93 NLS1s at $z < 0.1$, and M_{BH} estimates based on the updated mass estimators, we investigate the $M_{\text{BH}} - \sigma_*$ relation of NLS1s in comparison with broad-line AGNs. We find no strong evidence that the NLS1s deviates from the $M_{\text{BH}} - \sigma_*$ relation, which is defined by reverberation-mapped type 1 AGNs and quiescent galaxies. However, there is a clear trend of the offset with the host galaxy morphology, i.e., more inclined galaxies toward the line-of-sight have higher stellar velocity dispersion, suggesting that the rotational broadening plays a role in measuring stellar velocity dispersion based on the single-aperture spectra from the Sloan Digital Sky Survey. In addition, we provide the virial factor $\log f = 0.05 \pm 0.12$ ($f = 1.12$), for M_{BH} estimators based on the FWHM of $\text{H}\beta$, by jointly fitting the $M_{\text{BH}} - \sigma_*$ relation using quiescent galaxies and reverberation-mapped AGNs.

Subject headings: galaxies: active – galaxies: nuclei – galaxies: Seyfert

1. INTRODUCTION

The scaling relation between black hole mass and host-galaxy properties, e.g., the black hole mass–stellar velocity dispersion relation ($M_{\text{BH}} - \sigma_*$), suggests a coevolution of black holes and galaxies (e.g., Ferrarese & Merritt 2000; Gebhardt et al. 2000; Häring & Rix 2004; McConnell & Ma 2013; Kormendy & Ho 2013), motivating various theoretical and observational studies to constrain the origin of the scaling relations and their cosmic evolution (Bower et al. 2006; Croton 2006; Robertson et al. 2006; Treu et al. 2007; Woo et al. 2006, 2008; Bennert et al. 2011; Booth & Schaye 2011; Harris et al. 2012; Zhang et al. 2012; Park et al. 2014; Bennert et al. 2014). Along with inactive galaxies, galaxies hosting active galactic nuclei (AGN) also seem to follow the $M_{\text{BH}} - \sigma_*$ relation with a similar slope (e.g., Woo et al. 2010; Park et al. 2012; Woo et al. 2013), indicating that the present-day galaxies show a similar scaling relation regardless of black hole activity.

In contrast, it has been debated whether present-day narrow-line Seyfert 1 galaxies (NLS1s) deviate from the $M_{\text{BH}} - \sigma_*$ relation (e.g., Mathur et al. 2001; Komossa & Xu 2007). As a sub-class of AGNs, NLS1s were initially identified by the relatively small width of the broad-component of the Balmer lines ($\text{FWHM} < 2000 \text{ km s}^{-1}$) and a weak [O III]-to- $\text{H}\beta$ ratio ($[\text{O III}]/\text{H}\beta < 3$; Osterbrock & Pogge 1985). Since NLS1s are believed to have small black hole masses and high Eddington ratios (Boroson 2002), NLS1s are often considered as relatively young AGNs hosting black holes in a growing phase although the time evolution among various types of AGNs is highly uncertain. Thus, it is interesting to investigate the location of NLS1s in the $M_{\text{BH}} - \sigma_*$ plane in the context of black hole-galaxy coevolution.

A number of studies have been devoted to studying the $M_{\text{BH}} - \sigma_*$ relation of NLS1s over the last decade, result-

ing in a controversy. On the one hand, some studies claimed that NLS1 lie below the $M_{\text{BH}} - \sigma_*$ relation on average with smaller black hole masses at fixed stellar velocity dispersions, compared to the broad-line AGNs and quiescent galaxies (e.g., Mathur et al. 2001; Grupe & Mathur 2004; Mathur & Grupe 2005a,b; Bian et al. 2006; Zhou et al. 2006; Watson et al. 2007). On the other hand, other studies reported that the NLS1s are generally on the $M_{\text{BH}} - \sigma_*$ relation (e.g., Wang & Lu 2001; Komossa & Xu 2007). The fundamental limitation of the aforementioned studies is the fact that stellar velocity dispersions were not directly measured. Instead, the width of the narrow [O III] emission line at 5007\AA was used as a surrogate for stellar velocity dispersion, based on the empirical correlation between [O III] width and stellar velocity dispersion (Nelson 2000), although there is a considerably large scatter between them. If the ionized gas in the narrow-line region follows the gravitational potential of the host-galaxy, then [O III] line width can be substituted for stellar velocity dispersion. However for individual objects the uncertainty of this substitution is very large as shown by the direct comparison between [O III] width and the measured stellar velocity dispersion (e.g., Woo et al. 2006; Xiao et al. 2011). Moreover, the [O III] line often suffers from the effect of outflow, manifesting an asymmetric line profile and a strong blue-shifted wing component (e.g. Boroson 2005; Bae & Woo 2014). In this case, the width of the [O III] line will become much broader than stellar velocity dispersion, if the blue wing is not properly corrected for. In fact, Komossa & Xu (2007) showed that when the blue wing component is removed in measuring the width of the [O III] line, the inferred stellar velocity dispersion from [O III] becomes smaller, hence the NLS1 show a consistent $M_{\text{BH}} - \sigma_*$ relation compared to broad-line AGNs.

The solution to this decade-long debate is to investigate the locus of NLS1s in the $M_{\text{BH}} - \sigma_*$ plane, using *directly mea-*

measured stellar velocity dispersion. Although, measuring stellar velocity dispersion of AGN host galaxies is difficult due to the presence of strong AGN features, i.e., power-law continuum, Fe II emission, and broad emission lines, it is possible to measure stellar velocity dispersion if high quality spectra are available as demonstrated in a number of studies (e.g., Woo et al. 2006; Greene & Ho 2006; Woo et al. 2010; Hiner et al. 2012; Woo et al. 2013). In this paper, we present the direct stellar velocity dispersion measurements and estimates of black hole masses for a sample of 93 NLS1s at $z < 0.1$ selected from Sloan Digital Sky Survey Data Release 7 (SDSS DR7) (Abazajian et al. 2009), in order to investigate the $M_{\text{BH}} - \sigma_*$ relation of NLS1s. We describe the sample selection and properties in Section 2, and the analysis including mass determination and stellar velocity dispersion measurements in Section 3. Section 4 presents the results, followed by discussion in Section 5, and summary and conclusions in Section 6. Throughout the paper, we adopt a cosmology of $H_0 = 70 \text{ km s}^{-1} \text{ Mpc}^{-1}$, $\Omega_\Lambda = 0.7$ and $\Omega_m = 0.3$.

2. SAMPLE AND DATA

2.1. Sample selection

NLS1s are generally defined with two criteria: (1) the full-width-at-half-maximum (FWHM) of broad component of the Balmer lines $< 2000 \text{ km s}^{-1}$, and (2) the line flux ratio $[\text{O III}]/\text{H}\beta < 3$ (Osterbrock & Pogge 1985; Goodrich 1989). Additional characteristics of NLS1s include strong Fe II emission (Osterbrock & Pogge 1985), high Eddington ratio and soft X-ray emission (Leighly 1999; Grupe 2004; McHardy et al. 2006). In this study, we selected a sample of NLS1s from SDSS DR7 (Abazajian et al. 2009), based on the width of Balmer lines and the $[\text{O III}]/\text{H}\beta$ flux ratios. First, we selected NLS1 candidates by limiting the width of $\text{H}\beta$ to 500–2500 km s^{-1} , using the SpecLine class in the SDSS Query tool (<http://casjobs.sdss.org>). Since the line width measurements from the SDSS pipeline is not precise, we used a wider width range than the conventional definition for the initial selection, obtaining 4,252 NLS1 candidates at $z < 0.1$.

Second, using this initial sample, we performed a multi-component spectral decomposition analysis for each galaxy, to properly measure the width of the broad component of the Balmer lines. In the fitting process, we included multiple components, namely, featureless AGN continuum, stellar population model, and Fe II emission component, using an IDL-based spectral decomposition code (see Woo et al. 2006; Park et al. 2012, 2014). By subtracting the linear combination of featureless AGN continuum, stellar component and Fe II emission, we obtained emission line spectra and fit the broad and narrow emission lines (see section 3.1 for the detailed fitting process). Based on the measurements from the fitting process, we finalized a sample of 464 NLS1s, that satisfy the aforementioned two criteria by limiting the FWHM of broad $\text{H}\alpha$ between 800 and 2200 km s^{-1} and the line flux ratio $[\text{O III}]/\text{H}\beta$ less than 3.

Among these objects, we measured and collected the stellar velocity dispersion for 93 NLS1s. For 63 objects, we were able to directly measure stellar velocity dispersion using the SDSS spectra (see Section 3.5) while for 30 objects we obtained the stellar velocity dispersion measurements from Xiao et al. (2011). Thus, using this sample of 93 NLS1s, we investigate the properties of NLS1 and the $M_{\text{BH}} - \sigma_*$ relation. Note that the distribution of NLS1 properties (i.e., $[\text{O III}]/\text{H}\beta$ ratio, $\text{Fe II}/\text{H}\beta$ ratio, $\text{H}\alpha$ luminosity and width) of the final

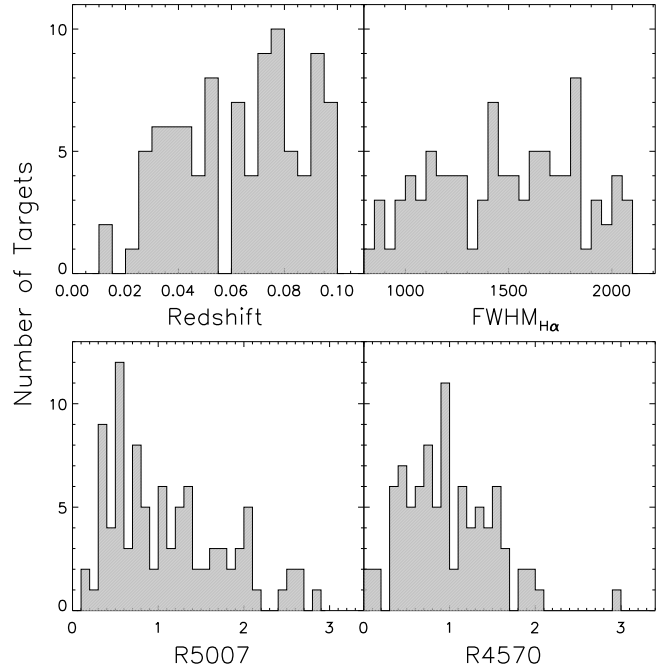


FIG. 1.— Histogram of the NLS1s showing the distribution of redshift, $\text{FWHM}_{\text{H}\alpha}$, R5007 and R4570. The $\text{H}\beta$ total flux is used to obtain R5007 and R4570.

sample of 93 objects is similar to that of the initial sample of 464 objects, suggesting that we may treat the final sample as a random subsample of NLS1 galaxy population.

2.2. Sample properties

Figure 1 presents the distributions of redshift and the width of $\text{H}\alpha$ of the final sample (top panels). To demonstrate the weak $[\text{O III}]$ emission and strong Fe II emission of the sample as the characteristic features of NLS1s (Osterbrock & Pogge 1985; Goodrich 1989; Véron-Cetty et al. 2001), we also present the distribution of the flux ratio $[\text{O III}]/\text{H}\beta$ (R5007) and $\text{Fe II}/\text{H}\beta$ (R4570) ratios in Figure 1 (bottom panels). Since the $\text{H}\beta$ is relatively weak and the decomposition of the broad and narrow components of $\text{H}\beta$ is uncertain, we used the total $\text{H}\beta$ flux to compare with $[\text{O III}]$ and Fe II fluxes.

In the case of the $[\text{O III}]$ strength (R5007), all galaxies in our sample show low $[\text{O III}]/\text{H}\beta$ ratio (< 3), with a median 1.05 and a mean 1.14. The Fe II strength (R4570), defined by the line flux ratio of Fe II emission integrated over the 4434–4684 Å region, to $\text{H}\beta$ (e.g., Véron-Cetty et al. 2001), is also high with a mean 1.06, as similarly found by other NLS1 studies (for dependence on the R4570 index, see §4.1). For example, Zhou et al. (2006) used the broad component of $\text{H}\beta$ to compare with Fe II and reported the mean R4570 as ~ 0.82 , while Xu et al. (2012) adopted the total flux of $\text{H}\beta$ and found the mean R4570 ~ 0.7 .

The M_{BH} estimated with the line dispersion of broad component of $\text{H}\alpha$ ranges over an order of magnitude, i.e., $\log M_{\text{BH}}/M_\odot = 5.84 - 7.38$ with a mean 6.72, which is comparable to that of the previous NLS1 $M_{\text{BH}} - \sigma_*$ relation studies (Grupe 2004; Komossa & Xu 2007). The Eddington ratio of our NLS1s ranges from 5% to the Eddington limit with a mean of 0.2–0.3, depending on the mass estimates.

3. ANALYSIS

3.1. Multi-component fitting of the emission lines

We performed multi-components spectral fitting analysis in two separate spectral ranges: $H\beta$ region (4400–5580Å) and $H\alpha$ region (6500–6800Å). For the $H\beta$ region, we followed the procedure given by our previous studies (Woo et al. 2006; McGill et al. 2008; Park et al. 2012, 2014; Woo et al. 2014, see also Barth et al. 2013). After converting all spectra to the rest frame, we modeled the observed spectra with three components, i.e., featureless AGN continuum, host-galaxy starlight, and Fe II emission blends, by respectively using a single power law continuum, a stellar population model based on the SED templates from Bruzual & Charlot (2003), and an Fe II template from (Boroson & Green 1992). The best continuum model was determined in the regions 4430–4600Å and 5080–5550Å, where Fe II emission dominates. We simultaneously fitted all 3 components, using the nonlinear Levenberg-Marquardt least-squares fitting routine *mpfit* (Markwardt 2009) in IDL. After subtracting the featureless AGN continuum and host-galaxy starlight from the raw spectra, emission line fitting for $H\beta$, [O III] $\lambda 4959$ and [O III] $\lambda 5007$ was carried out for this region. Since [O III] $\lambda 5007$ shows often complex profile such as velocity shift of [O III] core and asymmetry (Komossa & Xu 2007), we decomposed the [O III] line into a narrow core and a broad base. If [O III] has the broad base which tends to show blue-asymmetric (blue wing), the [O III] is fitted with double Gaussian components. On the other hand, if the [O III] profile is symmetric or of the S/N is low, the [O III] is fitted with a single Gaussian component. Then, the best-fit model of the [O III] $\lambda 5007$ line was used to model [O III] $\lambda 4959$ and $H\beta$ narrow component by assuming that these narrow lines have the same widths. The flux ratio of the [O III] $\lambda 4959$ to the [O III] $\lambda 5007$ was assumed to be 1:3, while the height of the $H\beta$ narrow component was set as free parameter. Next, we fitted the $H\beta$ broad component with a single Gaussian component since the S/N of $H\beta$ is typically lower than [O III].

For the $H\alpha$ region, we did not subtract Fe II emission because Fe II is relatively weak in this spectral range. First, we fit the host-galaxy continuum using two spectral regions 6400–6460Å and 6740–6800Å for determining the best model, where no other emissions are present. After subtracting the stellar features, we fitted [S II] $\lambda 6716$ and [S II] $\lambda 6731$, respectively with a single Gaussian component. We assumed that the widths of [S II], [N II], and the $H\alpha$ narrow component are the same, and used the width of the [S II] for fitting [N II] and the narrow $H\alpha$, if the spectral quality is high (S/N of [S II] > 25). For low S/N targets, the width of [S II] is not reliable and we fitted the $H\alpha$ narrow component and the [N II] doublet with a single Gaussian model, without using the best-fit of the [S II] line. The flux ratio between [N II] $\lambda 6548$ and [N II] $\lambda 6583$ is assumed as 1/3. For the $H\alpha$ broad component, Gauss-Hermitian series were used to model the $H\alpha$ profile as done by McGill et al. (2008). Figure 2 presents an example of the multicomponent fitting.

We estimated the uncertainty of the $H\alpha$ luminosity based on the S/N of the line flux. In the case of the line widths, we performed Monte Carlo simulations by randomizing the flux per pixel using the flux noise. For a set of 100 simulated spectra, we repeated spectral decomposition, measured the line width, and adopted the 1-sigma dispersion of the distribution as the uncertainty of the line widths for each object. The estimated uncertainties are included in Table 1.

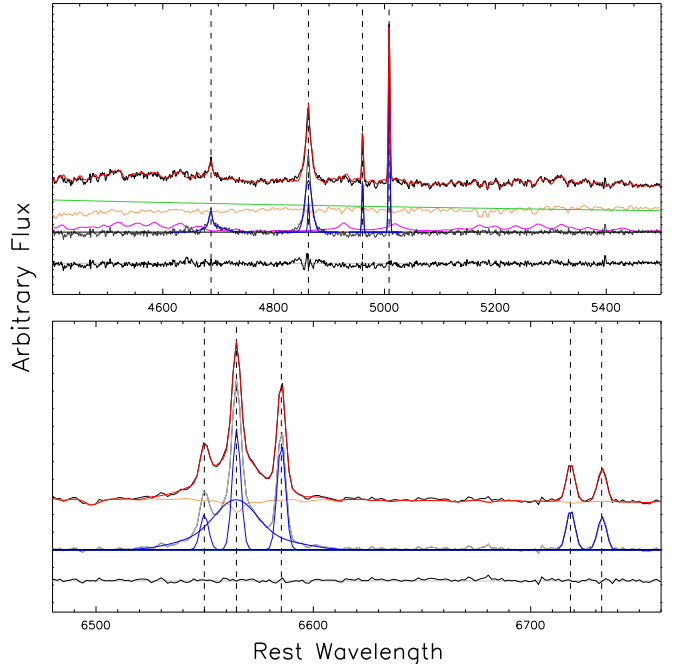


FIG. 2.— Example of multi-component spectral fitting for the $H\beta$ (top) and $H\alpha$ region (bottom). In both panels, raw spectra (black) and the best-fit of total models (red) are illustrated in upper part, and the best-fit of emission lines (blue), power-law continuum (green), host-galaxy spectrum (orange) are shown in the bottom part. For the $H\beta$ region, Fe II blend model (magenta) is presented additionally. The residuals (black) are arbitrarily shifted downward to clarify.

3.2. Black hole mass

Black hole mass can be determined based on the virial theorem:

$$M_{\text{BH}} = f \frac{V^2 R_{\text{BLR}}}{G} \quad (1)$$

where V is the velocity of the broad-line region (BLR) gas, R_{BLR} is the BLR size, and G is the gravitational constant (Peterson et al. 2004). Generally, either the second moment (line dispersion; $\sigma_{H\beta}$) or the FWHM of the $H\beta$ line ($\text{FWHM}_{H\beta}$) is used for the velocity of the BLR gas. Along with each velocity measurements, a virial factor f is needed for mass determination. The determination of the average virial factor, respectively, for $\sigma_{H\beta}$ and $\text{FWHM}_{H\beta}$ can be found in Appendix, where we derived the virial factor by comparing the reverberation-mapped AGNs and quiescent galaxies in the $M_{\text{BH}} - \sigma_*$ plane.

Instead of directly measuring the size of BLR by reverberation mapping, which requires a long-term spectroscopic monitoring, an empirical size-luminosity relation (e.g., Kaspi et al. 2000, 2005; Bentz et al. 2009b, 2013) has been used for M_{BH} estimates. We used the size-luminosity relation from Bentz et al. (2013), and derive the M_{BH} estimator as follows,

$$M_{\text{BH}} = f \times 10^{6.819} \left(\frac{\sigma_{H\beta}}{10^3 \text{ km s}^{-1}} \right)^2 \left(\frac{\lambda L_{5100}}{10^{44} \text{ erg s}^{-1}} \right)^{0.533} M_{\odot} . \quad (2)$$

For our NLS1s, the width of the $H\alpha$ line is better determined than that of the $H\beta$ lines since $H\beta$ often have much lower S/N. Thus, we used the measurement of $H\alpha$ line width and luminosity for M_{BH} estimation, using the following two

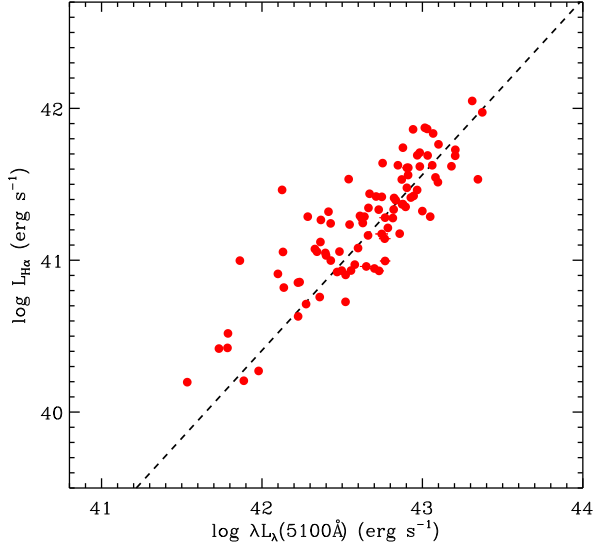


FIG. 3.— Comparison between L_{5100} and $H\alpha$ luminosity of the NLS1s. The dashed line represents the derived relation by citeGH2005.

relations (Greene & Ho 2005):

$$\text{FWHM}_{H\beta} = (1.07 \pm 0.07) \times 10^3 \left(\frac{\text{FWHM}_{H\alpha}}{10^3 \text{ km s}^{-1}} \right)^{(1.03 \pm 0.03)} \text{ km s}^{-1} \quad (3)$$

$$L_{H\alpha} = (5.25 \pm 0.02) \times 10^{42} \left(\frac{\lambda L_{5100}}{10^{44} \text{ erg s}^{-1}} \right)^{(1.157 \pm 0.005)} \text{ erg s}^{-1} \quad (4)$$

Assuming the $H\beta$ and $H\alpha$ have the same line profile (i.e., $\text{FWHM} = 2\sigma$), we also converted $\sigma_{H\alpha}$ to $\sigma_{H\beta}$ using Eq. 3. To test the validity of Eq. 3 for our NLS1, we compared the line width of $H\beta$ and $H\alpha$ using a subsample of 41 NLS1s, for which the S/N ratio of $H\beta$ is larger than 20 so that we could obtain reliable emission line fitting results. We find that the relation between $H\alpha$ and $H\beta$ of NLS1s is consistent with that of reported by Greene & Ho (2005), with a slight offset 0.041 ± 0.009 from the equation (3). For comparing L_{5100} with $H\alpha$ luminosity, we used all NLS1s in our sample, for which L_{5100} was measured from a power-law component in the multi-component fitting process. As shown in Figure 3, the relation between L_{5100} and $H\alpha$ luminosity is close to Equation (4), with a slight offset 0.077 ± 0.202 . This result suggests that using the conversion equation is acceptable for NLS1s and that the multi-component fitting results are reasonable, although a proper comparison is difficult due to the limited dynamical range of the NLS1 sample compared to that of Greene & Ho (2005). Note that we used a Gauss-Hermite series for the broad $H\alpha$ component, and a single Gaussian model for the broad $H\beta$ component (due to low S/N ratio), while Greene & Ho (2005) used a multicomponent Gaussian models for both $H\alpha$ and $H\beta$. The difference of the fitting model may be partly responsible for the slight systematic offset.

We derived a black hole mass estimators by combining aforementioned scaling relations as:

$$M_{\text{BH}} = f \times 10^{6.544} \left(\frac{L_{H\alpha}}{10^{42} \text{ erg s}^{-1}} \right)^{0.46} \left(\frac{\text{FWHM}_{H\alpha}}{10^3 \text{ km s}^{-1}} \right)^{2.06} M_{\odot}, \quad (5)$$

$$M_{\text{BH}} = f \times 10^{6.561} \left(\frac{L_{H\alpha}}{10^{42} \text{ erg s}^{-1}} \right)^{0.46} \left(\frac{\sigma_{H\alpha}}{10^3 \text{ km s}^{-1}} \right)^{2.06} M_{\odot}. \quad (6)$$

We adopted $\log f = 0.05 \pm 0.12$ ($f = 1.12$) for FWHM-based M_{BH} while we used $\log f = 0.65 \pm 0.12$ ($f = 4.47$) for σ -based M_{BH} (see Appendix for detailed discussion).

3.3. Stellar velocity dispersion

Directly measuring stellar velocity dispersions is a key to determine the location of NLS1 on the $M_{\text{BH}} - \sigma_*$ plane. To investigate the systematic uncertainties of the stellar velocity dispersion measurements, we measured σ_* in three spectral regions: (1) Mg b -Fe region (5000-5430Å), which includes strong absorption lines, i.e., Mg b triplet (5069, 5154, 5160Å) and Fe (5270, 5335Å) lines (hereafter σ_{Mgb}); (2) Mg b -Fe region (5000-5430Å) excluding the Mg b triplet (hereafter σ_{noMgb}); and (3) Ca II region (8400-8800Å), where the Ca II triplet (8498, 8542, 8662Å) is a strong feature (hereafter σ_{CaT}). The line strength of the Mg b triplet is much higher in the composite spectra of massive elliptical galaxies than in the nearby stars, hence, the template mismatch due to the α -element enhancement can potentially cause a systematic bias in measuring σ_* , although this effect is not significant for late-type host galaxies (Barth et al. 2002, 2003; Woo et al. 2004, 2005). In the case of the Ca II triplet region, AGN contamination (e.g., Fe II emission) is relatively weaker than the Mg b region, while the residual of sky emission lines is often present and the quality of spectra is generally lower than that of the Mg b region. Thus, as a consistency check, we measured stellar velocity dispersion using three different spectral regions (see similar investigation by Greene et al. 2005). We find that three measurements are consistent, showing that the effect of the Mg abundance is negligible (see below).

We corrected for the SDSS spectral resolution by subtracting the instrumental resolution from the measured stellar velocity dispersion in quadrature. Instead of using a mean constant resolution $\sim 70 \text{ km s}^{-1}$, which is often adopted in the literature, we calculated the mean instrumental resolution in the corresponding fitting ranges for each object, using the spectral resolution fits file provided by SDSS DR7. For example, we used the spectral range 5000-5430 Å to calculate the mean instrumental resolution for the Mg b -Fe region, which is ~ 55 -56 km s^{-1} . Compared to the instrumental resolution, the stellar lines of the objects that we measured stellar velocity dispersions are well resolved.

After masking out AGN narrow emission lines (e.g., [Fe VII] $\lambda 5160$, [N I] $\lambda 5201$, [Ca V] $\lambda 5310$; Vanden Berk et al. 2001), we measured σ_* by using both the penalized pixel-fitting (pPXF) method (Cappellari & Emsellem 2004) and a Python-based code based on the algorithm by van der Marel (1994). We used stellar velocity templates from INDO-US stellar library, which includes various spectral type giant stars with a range of metallicity ($[\text{Fe}/\text{H}] = -0.49 - 0.18$) (Valdes et al. 2004). Low order polynomials were used to fit the broad curvature in the spectra after masking out the narrow emission lines and bad spectral regions. After intense tests with various polynomial orders and templates for each target, we adopted the mean of the measurements based on each polynomial order and each spectral range with a different mask-out region, as a final measurement of σ_* .

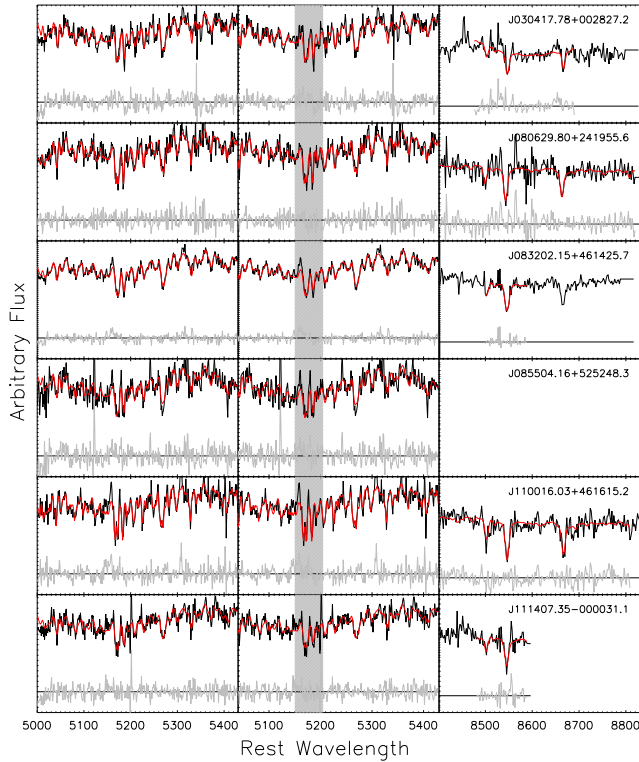


FIG. 4.— Examples of stellar velocity dispersion fitting using the Mg b-Fe region (left) by excluding the Mg b triplet line (middle), and the Ca II region (right). The observed spectrum (black line) is overplotted with the best-fit model (red line) in each panel while the residual of the fit (gray) is shown at the bottom.

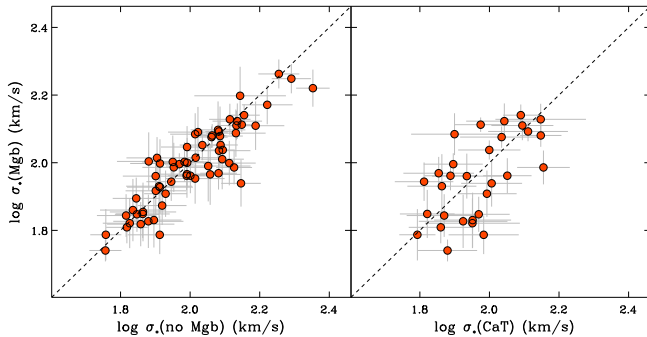


FIG. 5.— Comparisons between the measurements of stellar velocity dispersion. The relations of σ_{Mgb} with σ_{noMgb} for 93 NLS1s (left) and with σ_{CaT} for 34 NLS1s (right) are illustrated.

In this process, we measured σ_{Mgb} for 62 NLS1s, that show strong enough stellar lines. Among them, we were able to measure σ_{CaT} for 34 NLS1s, while we could not measure the σ_* from the Ca II triplet for the other objects, since the SDSS spectral range does not cover the rest-frame Ca II triplet region for targets at $z > 0.082$, or the strength of the Ca II triplet is too weak to measure σ_* (see Figure 4). As a consistency check, we compared the σ_{Mgb} with σ_{noMgb} and σ_{CaT} in Figure 5. The σ_{Mgb} is slightly higher by a few percent (0.015 dex) than the σ_{noMgb} , and the rms scatter is 0.06 dex. This result confirms

the σ_{Mgb} is consistent with the σ_{noMgb} and indicates the influence of the Mg b triplet is marginal in measuring the σ_* of the host galaxies of NLS1s. The comparison between σ_{CaT} and σ_{Mgb} shows slightly larger scatter (0.10 dex), but the average offset is still close to zero (i.e., 0.014 dex), suggesting that the σ_{Mgb} is consistent with the σ_{CaT} . Based on these results without strong bias among the measurements from various spectral regions, we adopted σ_{Mgb} as the final measurements. As a consistency check, we compared our measurements with SDSS DR7 values. We found stellar velocity dispersion measurements for 5 objects from SDSS DR7, which are consistent with our measurements within the measurement uncertainties.

Among 93 NLS1s, 30 NLS1s were studied previously by Xiao et al. (2011), who measured σ_* based on high quality spectra with higher spectral resolution obtained with the Keck Echelle Spectrograph and Imager (ESI) and the Magellan Echelle (MagE). Thus, including the σ_* measurements of 30 NLS1s from Xiao et al. (2011), we have a total of 93 measurements of the σ_* . We note that the 3'' SDSS fiber size is larger than the slit size adopted by Xiao et al. (2011). Thus, the SDSS spectra represent a larger physical scale of the host galaxies than the Keck spectra of Xiao et al. (2011), and may show larger influence of rotational broadening. However, it is difficult to perform a direct comparison between SDSS-based and Keck-based measurements due to the fact that most of 30 NLS1s studied by Xiao et al. (2011) have smaller velocity dispersion than the SDSS instrumental resolution. We found only one object among 30 NLS1s, for which both SDSS-based and Keck-based stellar velocity dispersion measurements are available and show consistency (75 ± 10 vs. 71 ± 5 km s $^{-1}$).

3.4. Morphology classification

For galaxies with a rotating stellar disk, the line-of-sight stellar velocity dispersion can be overestimated due to rotational broadening (Bennert et al. 2011; Harris et al. 2012; Kang et al. 2013), therefore it is important to correct for the rotation effect in measuring σ_* . Since the rotating disk is common among late-type galaxies and the ratio between rotation velocity and velocity dispersion is typically higher in late-type galaxies than in early-type galaxies, the effect of the rotational broadening is expected to be stronger for late type galaxies, particularly for more inclined galaxies toward the line-of-sight.

To investigate the rotation effect on the $M_{\text{BH}} - \sigma_*$ relation, we classified our NLS1s into early and late type galaxies, using the SDSS colors and the presence of a disk. For late-type galaxies, we further divided them into two groups: more face-on and more edge-on galaxies based on the inclination of the disk. The inclination angle is determined from the minor-to-major axial ratio of the disk as $i = \sin^{-1}q$, where i is the inclination angle of the galactic disk to the line of sight (i.e., $i = 0^\circ$ for an edge-on disk) and q is the ratio of the minor to major axes of the disk. We classified our sample with $q > 0.5$ (i.e., $i > 30^\circ$) as face-on galaxies, and the others with $q < 0.5$ (i.e., $i < 30^\circ$) were classified as edge-on galaxies. As a result, 93 NLS1 galaxies were divided into 35 early type galaxies and 58 late type galaxies which were further divided into 48 face-on and 10 edge-on late types.

TABLE 1
NLS1

Name	z	$\log L_{\text{H}\alpha}$ (erg s^{-1})	$\sigma_{\text{H}\alpha}$ (km s^{-1})	$\text{FWHM}_{\text{H}\alpha}$ (km s^{-1})	$\log M_{\text{BH}}(\sigma_{\text{H}\alpha})$ (M_{\odot})	$\log M_{\text{BH}}(\text{FWHM}_{\text{H}\alpha})$ (M_{\odot})	σ_* (km s^{-1})	S/N
(1)	(2)	(3)	(4)	(5)	(6)	(7)	(8)	(9)
J010409.16+000843.6	0.071	41.29 ± 0.01	701 ± 11	1375 ± 28	6.57 ± 0.02	6.55 ± 0.02	66 ± 16	15
J030417.78+002827.2	0.045	41.40 ± 0.01	728 ± 11	1248 ± 19	6.65 ± 0.01	6.51 ± 0.01	88 ± 8	30
J073106.86+392644.5	0.048	41.06 ± 0.01	662 ± 7	1185 ± 19	6.41 ± 0.01	6.31 ± 0.01	72 ± 14	19
J073714.28+292634.1	0.080	41.46 ± 0.01	966 ± 26	1553 ± 36	6.93 ± 0.03	6.74 ± 0.03	102 ± 12	19
J080253.18+130559.6	0.095	42.05 ± 0.01	1072 ± 8	1903 ± 21	7.30 ± 0.01	7.19 ± 0.01	97 ± 17	24
J080538.22+244214.8	0.099	41.61 ± 0.02	784 ± 14	1242 ± 94	6.81 ± 0.02	6.61 ± 0.02	102 ± 24	11
J080801.75+381935.3	0.041	40.86 ± 0.01	896 ± 21	1683 ± 41	6.59 ± 0.02	6.53 ± 0.02	100 ± 12	20
J081718.55+520147.7	0.039	41.06 ± 0.01	842 ± 12	1486 ± 32	6.62 ± 0.01	6.51 ± 0.01	68 ± 14	18
J082007.81+372839.6	0.082	41.42 ± 0.01	1085 ± 61	1661 ± 92	7.02 ± 0.05	6.78 ± 0.05	141 ± 17	22
J083202.15+461425.7	0.046	41.42 ± 0.01	1026 ± 20	1646 ± 42	6.97 ± 0.02	6.77 ± 0.02	128 ± 5	38
J083741.94+263344.1	0.076	41.34 ± 0.01	1025 ± 44	1767 ± 131	6.93 ± 0.04	6.80 ± 0.04	105 ± 16	17
J083949.65+484701.4	0.039	41.56 ± 0.01	904 ± 9	1495 ± 14	6.92 ± 0.01	6.75 ± 0.01	112 ± 6	42
J084927.36+324852.8	0.064	41.64 ± 0.01	1235 ± 23	2045 ± 33	7.23 ± 0.02	7.07 ± 0.02	137 ± 11	25
J085504.16+525248.3	0.089	41.86 ± 0.01	889 ± 20	1540 ± 32	7.04 ± 0.02	6.92 ± 0.02	103 ± 10	20
J092438.88+560746.8	0.026	41.00 ± 0.01	899 ± 18	1723 ± 38	6.66 ± 0.02	6.62 ± 0.02	146 ± 5	39
J093638.69+132529.6	0.090	41.41 ± 0.01	1025 ± 44	1916 ± 209	6.96 ± 0.04	6.91 ± 0.04	102 ± 11	17
J094153.41+163621.0	0.052	41.05 ± 0.01	1005 ± 17	2078 ± 39	6.78 ± 0.02	6.81 ± 0.02	101 ± 11	15
J095848.67+025243.2	0.079	41.07 ± 0.01	1004 ± 30	1710 ± 51	6.79 ± 0.03	6.65 ± 0.03	117 ± 11	18
J100854.93+373929.9	0.054	41.97 ± 0.01	1010 ± 20	1750 ± 52	7.21 ± 0.02	7.08 ± 0.02	105 ± 9	38
J102532.09+102503.9	0.046	41.29 ± 0.01	930 ± 9	1615 ± 20	6.82 ± 0.01	6.70 ± 0.01	111 ± 8	26
J103103.52+462616.8	0.093	41.86 ± 0.01	1029 ± 15	1806 ± 30	7.17 ± 0.01	7.06 ± 0.01	169 ± 16	21
J103751.81+334850.1	0.051	40.82 ± 0.01	1053 ± 49	1832 ± 72	6.71 ± 0.04	6.59 ± 0.04	94 ± 12	18
J104153.59+031500.6	0.093	41.69 ± 0.01	1155 ± 20	1940 ± 35	7.20 ± 0.02	7.04 ± 0.02	126 ± 21	18
J105600.39+165626.2	0.085	41.48 ± 0.01	996 ± 24	1821 ± 42	6.97 ± 0.02	6.89 ± 0.02	126 ± 15	20
J110016.03+461615.2	0.032	40.91 ± 0.01	835 ± 11	1646 ± 20	6.55 ± 0.01	6.54 ± 0.01	68 ± 6	24
J111253.12+314807.3	0.076	41.87 ± 0.01	1291 ± 20	2049 ± 35	7.38 ± 0.02	7.18 ± 0.02	72 ± 18	16
J111407.35-000031.1	0.073	41.41 ± 0.01	954 ± 23	1519 ± 33	6.90 ± 0.02	6.70 ± 0.02	125 ± 10	25
J112229.65+214815.5	0.061	41.44 ± 0.01	994 ± 16	1683 ± 36	6.95 ± 0.02	6.80 ± 0.02	125 ± 7	29
J112229.65+214815.5	0.100	41.71 ± 0.01	1318 ± 75	2027 ± 70	7.32 ± 0.05	7.09 ± 0.05	176 ± 20	21
J112545.34+240823.9	0.024	40.20 ± 0.01	688 ± 16	1211 ± 33	6.05 ± 0.02	5.94 ± 0.02	82 ± 8	25
J113101.10+134539.6	0.092	41.83 ± 0.01	1087 ± 26	1826 ± 37	7.21 ± 0.02	7.06 ± 0.02	171 ± 14	26
J113111.93+100231.3	0.074	41.25 ± 0.02	930 ± 33	1785 ± 112	6.80 ± 0.03	6.77 ± 0.03	130 ± 18	14
J113913.91+335551.1	0.033	41.53 ± 0.01	834 ± 19	1394 ± 48	6.84 ± 0.02	6.68 ± 0.02	112 ± 15	32
J115333.22+095408.4	0.069	41.62 ± 0.01	983 ± 16	1844 ± 35	7.02 ± 0.02	6.97 ± 0.02	130 ± 11	25
J120012.47+183542.9	0.066	40.92 ± 0.01	862 ± 47	1571 ± 61	6.58 ± 0.05	6.50 ± 0.05	136 ± 13	19
J121157.48+055801.1	0.068	41.74 ± 0.01	1012 ± 13	1984 ± 36	7.10 ± 0.01	7.09 ± 0.01	119 ± 12	22
J122307.79+192337.0	0.076	41.33 ± 0.01	1079 ± 35	1832 ± 101	6.97 ± 0.03	6.83 ± 0.03	122 ± 12	21
J123651.17+453904.1	0.030	41.24 ± 0.01	863 ± 16	1601 ± 47	6.73 ± 0.02	6.67 ± 0.02	97 ± 7	29
J123932.59+342221.3	0.084	41.53 ± 0.01	898 ± 56	1540 ± 109	6.90 ± 0.06	6.77 ± 0.06	84 ± 7	32
J124319.97+025256.1	0.087	41.69 ± 0.01	752 ± 16	1276 ± 29	6.81 ± 0.02	6.67 ± 0.02	112 ± 12	26
J130456.96+395529.7	0.028	40.42 ± 0.01	915 ± 34	1431 ± 124	6.40 ± 0.03	6.19 ± 0.03	92 ± 6	23
J131142.56+331612.7	0.078	41.29 ± 0.01	1145 ± 33	2086 ± 41	7.01 ± 0.03	6.93 ± 0.03	106 ± 14	16
J131305.81+012755.9	0.029	40.85 ± 0.01	868 ± 12	1599 ± 28	6.56 ± 0.01	6.49 ± 0.01	108 ± 5	36
J131905.95+310852.7	0.032	40.97 ± 0.01	1391 ± 38	2063 ± 61	7.03 ± 0.03	6.77 ± 0.03	137 ± 6	38
J134240.09+022524.4	0.075	41.03 ± 0.01	956 ± 57	1842 ± 60	6.73 ± 0.05	6.70 ± 0.05	105 ± 14	16
J134401.90+255628.3	0.062	41.33 ± 0.01	1068 ± 58	1651 ± 43	6.96 ± 0.05	6.74 ± 0.05	140 ± 9	25
J140659.58+231738.6	0.061	40.73 ± 0.01	965 ± 48	1400 ± 87	6.59 ± 0.05	6.31 ± 0.05	97 ± 8	26
J141434.52+293428.2	0.076	41.29 ± 0.01	844 ± 29	1376 ± 39	6.73 ± 0.03	6.55 ± 0.03	75 ± 15	20
J143658.68+164513.6	0.072	40.93 ± 0.01	770 ± 24	1418 ± 55	6.49 ± 0.03	6.42 ± 0.03	73 ± 10	17
J143708.46+074013.6	0.087	41.24 ± 0.01	1089 ± 45	1956 ± 66	6.94 ± 0.04	6.84 ± 0.04	98 ± 13	16
J151356.88+481012.1	0.079	41.63 ± 0.01	737 ± 30	1270 ± 55	6.77 ± 0.04	6.64 ± 0.04	124 ± 16	21
J152209.56+451124.0	0.066	41.32 ± 0.01	900 ± 28	1886 ± 251	6.80 ± 0.03	6.85 ± 0.03	128 ± 12	18
J152324.42+551855.3	0.039	41.12 ± 0.01	1086 ± 34	1717 ± 91	6.88 ± 0.03	6.67 ± 0.03	128 ± 7	33
J152940.58+302909.3	0.036	41.69 ± 0.01	1073 ± 22	1823 ± 54	7.13 ± 0.02	6.99 ± 0.02	107 ± 5	44
J155640.90+121717.9	0.036	41.05 ± 0.01	1131 ± 26	2002 ± 35	6.88 ± 0.02	6.78 ± 0.02	149 ± 9	30
J160746.00+345048.9	0.054	41.53 ± 0.01	749 ± 7	1422 ± 14	6.74 ± 0.01	6.69 ± 0.01	80 ± 10	28
J161527.67+403153.6	0.084	41.35 ± 0.01	868 ± 39	1608 ± 54	6.79 ± 0.04	6.72 ± 0.04	137 ± 18	17
J161809.36+361957.8	0.034	41.16 ± 0.01	578 ± 11	896 ± 27	6.34 ± 0.02	6.11 ± 0.02	87 ± 8	30
J161951.31+405847.3	0.038	41.27 ± 0.01	1020 ± 15	1746 ± 26	6.89 ± 0.01	6.76 ± 0.01	114 ± 10	26
J162930.01+420703.2	0.072	41.37 ± 0.01	816 ± 14	1440 ± 36	6.74 ± 0.02	6.63 ± 0.02	101 ± 11	22
J163501.46+305412.1	0.054	41.63 ± 0.01	854 ± 40	1261 ± 145	6.90 ± 0.04	6.63 ± 0.04	130 ± 14	23
J210226.54+000702.3	0.052	40.76 ± 0.01	806 ± 45	1466 ± 46	6.45 ± 0.05	6.37 ± 0.05	96 ± 14	15
J210533.44+002829.3	0.054	41.21 ± 0.01	853 ± 17	1429 ± 27	6.71 ± 0.02	6.55 ± 0.02	81 ± 9	23
J010712.03+140844.9	0.077	41.42 ± 0.01	597 ± 184	998 ± 170	6.48 ± 0.28	6.32 ± 0.28	38 ± 4 ^a	15
J024912.86-081525.7	0.030	40.21 ± 0.01	542 ± 19	915 ± 46	5.84 ± 0.03	5.69 ± 0.03	53 ± 3 ^a	18
J080629.80+241955.6	0.041	40.71 ± 0.01	629 ± 19	1067 ± 39	6.20 ± 0.03	6.06 ± 0.03	71 ± 5 ^a	20
J080907.57+441641.4	0.054	40.90 ± 0.01	692 ± 27	1150 ± 42	6.38 ± 0.04	6.22 ± 0.04	65 ± 3 ^a	21
J081550.23+250640.9	0.073	40.93 ± 0.02	568 ± 61	895 ± 90	6.21 ± 0.10	6.00 ± 0.10	65 ± 2 ^a	12
J082912.68+500652.3	0.044	41.28 ± 0.01	597 ± 7	1002 ± 16	6.42 ± 0.01	6.26 ± 0.01	60 ± 2 ^a	29
J094057.19+032401.2	0.061	41.46 ± 0.01	738 ± 21	1206 ± 45	6.69 ± 0.03	6.51 ± 0.03	82 ± 3 ^a	20
J094529.36+093610.4	0.013	40.52 ± 0.01	907 ± 11	1767 ± 27	6.44 ± 0.01	6.42 ± 0.01	76 ± 2 ^a	34
J095151.82+060143.6	0.093	41.00 ± 0.02	742 ± 100	1192 ± 139	6.48 ± 0.12	6.29 ± 0.12	76 ± 6 ^a	11
J101627.33-000714.5	0.094	41.17 ± 0.03	648 ± 34	1109 ± 90	6.44 ± 0.05	6.31 ± 0.05	55 ± 7 ^a	8
J102348.44+040553.7	0.099	40.96 ± 0.02	812 ± 181	869 ± 108	6.55 ± 0.20	5.99 ± 0.20	91 ± 13 ^a	9

TABLE 1 — *Continued*

Name	z	$\log L_{H\alpha}$ (erg s^{-1})	$\sigma_{H\alpha}$ (km s^{-1})	$\text{FWHM}_{H\alpha}$ (km s^{-1})	$\log M_{\text{BH}}(\sigma_{H\alpha})$ (M_{\odot})	$\log M_{\text{BH}}(\text{FWHM}_{H\alpha})$ (M_{\odot})	σ_* (km s^{-1})	S/N
(1)	(2)	(3)	(4)	(5)	(6)	(7)	(8)	(9)
J111031.61+022043.2	0.079	41.37 ± 0.01	671 ± 15	1100 ± 30	6.56 ± 0.02	6.39 ± 0.02	77 ± 3^a	16
J112526.51+022039.0	0.049	41.00 ± 0.01	843 ± 30	1305 ± 48	6.60 ± 0.03	6.37 ± 0.03	87 ± 5^a	20
J114339.49-024316.3	0.094	41.32 ± 0.01	746 ± 40	1192 ± 72	6.64 ± 0.05	6.44 ± 0.05	97 ± 5^a	22
J121518.23+014751.1	0.071	41.28 ± 0.01	636 ± 22	1036 ± 38	6.47 ± 0.03	6.29 ± 0.03	81 ± 3^a	18
J122342.82+581446.2	0.015	40.42 ± 0.01	706 ± 13	1049 ± 32	6.17 ± 0.02	5.91 ± 0.02	45 ± 2^a	26
J124035.82-002919.4	0.081	41.76 ± 0.01	728 ± 11	1133 ± 31	6.82 ± 0.02	6.60 ± 0.02	56 ± 3^a	19
J125055.28-015556.7	0.081	41.51 ± 0.02	849 ± 21	1428 ± 73	6.84 ± 0.02	6.69 ± 0.02	66 ± 4^a	15
J131926.52+105610.9	0.064	41.55 ± 0.01	671 ± 13	1040 ± 31	6.65 ± 0.02	6.42 ± 0.02	47 ± 3^a	23
J143450.62+033842.5	0.028	40.27 ± 0.01	708 ± 34	1289 ± 54	6.11 ± 0.04	6.03 ± 0.04	57 ± 3^a	22
J144052.60-023506.2	0.045	41.18 ± 0.01	674 ± 18	1087 ± 43	6.48 ± 0.03	6.29 ± 0.03	73 ± 8^a	28
J144705.46+003653.2	0.096	41.14 ± 0.02	924 ± 44	1495 ± 56	6.75 ± 0.04	6.56 ± 0.04	64 ± 4^a	9
J145045.54-014752.9	0.099	41.62 ± 0.01	1086 ± 96	1690 ± 250	7.11 ± 0.08	6.89 ± 0.08	138 ± 6^a	17
J155005.95+091035.7	0.092	41.73 ± 0.01	572 ± 37	988 ± 121	6.59 ± 0.06	6.46 ± 0.06	78 ± 6^a	18
J162636.40+350242.1	0.034	40.63 ± 0.01	578 ± 21	828 ± 35	6.09 ± 0.03	5.80 ± 0.03	52 ± 1^a	24
J163159.59+243740.2	0.044	41.08 ± 0.01	649 ± 10	958 ± 20	6.40 ± 0.02	6.13 ± 0.02	66 ± 2^a	24
J172759.14+542147.0	0.100	41.28 ± 0.02	668 ± 39	1055 ± 80	6.52 ± 0.05	6.31 ± 0.05	67 ± 8^a	8
J205822.14-065004.3	0.074	41.61 ± 0.01	655 ± 8	1101 ± 19	6.65 ± 0.01	6.50 ± 0.01	58 ± 3^a	17
J221139.16-010534.9	0.092	40.95 ± 0.02	604 ± 50	1104 ± 64	6.28 ± 0.07	6.20 ± 0.07	68 ± 7^a	10
J230649.77+005023.3	0.061	40.93 ± 0.01	851 ± 46	1508 ± 48	6.58 ± 0.05	6.47 ± 0.05	65 ± 3^a	16

Notes. Column 1: galaxy name; Column 2: redshift; Column 3: luminosity of $H\alpha$; Column 4: line dispersion of $H\alpha$; Column 5: FWHM of $H\alpha$; Column 6: black hole mass calculated using $\sigma_{H\alpha}$. The errors represent the propagated errors from the uncertainties of the line width and luminosity, without considering systematic errors, e.g., the scatter of the size-luminosity relation, the uncertainty of the virial factor, etc; Column 7: black hole mass calculated using FWHM $_{H\alpha}$; Column 8: stellar velocity dispersion; Column 8: signal-to-noise ratio at 5100Å of the SDSS spectra.

^a Stellar velocity dispersions are taken from Xiao et al. (2011).

4. RESULT

4.1. $M_{\text{BH}}-\sigma_*$ relation of NLS1s

We compare the 93 NLS1 with the RM AGNs and quiescent galaxies in the $M_{\text{BH}}-\sigma_*$ plane in Figure 4. In the left panel, M_{BH} is determined using the line dispersion of the Balmer lines and the virial factor $\log f = 0.65$, while M_{BH} in the right panel is estimated using the FWHM of the Balmer lines and the virial factor $\log f = 0.05$ (see appendix for the determination of the virial factors). In general, NLS1s seem to show a consistent $M_{\text{BH}}-\sigma_*$ relation compared to the RM AGNs. With respect to the best-fit $M_{\text{BH}}-\sigma_*$ relation obtained for the joint sample of the RM AGNs and quiescent galaxies (solid line), the average offset of the NLS1s is $\Delta \log M_{\text{BH}} = 0.04 \pm 0.06$ in the left panel, and $\Delta \log M_{\text{BH}} = -0.08 \pm 0.06$ in the right panel, suggesting that NLS1s follow the same $M_{\text{BH}}-\sigma_*$ relation as other local galaxies. When we compare NLS1s with the best-fit $M_{\text{BH}}-\sigma_*$ relation of quiescent galaxies, we obtained almost the same result since the best-fit $M_{\text{BH}}-\sigma_*$ relation is almost identical between quiescent sample and the joint sample of quiescent and RM AGNs since the quiescent galaxies are dominant in terms of number and dynamical range (for details, see Woo et al. 2013).

Similarly, when we compare NLS1s with the best-fit $M_{\text{BH}}-\sigma_*$ relation of the RM AGNs only (dashed line), we obtain a slightly increased offset $\Delta \log M_{\text{BH}} = -0.11 \pm 0.04$ and $\Delta \log M_{\text{BH}} = -0.19 \pm 0.05$, respectively for σ -based M_{BH} and FWHM-based M_{BH} . The best-fit $M_{\text{BH}}-\sigma_*$ relation of the RM AGNs suffers from the effect of the limited mass distribution compared to the quiescent galaxy sample. The truncation of the mass distribution of the RM AGNs caused a shallower slope of the $M_{\text{BH}}-\sigma_*$ relation as discussed in detail by Woo et al. 2013. In turn, the offset of the NLS1s with respect to

this shallow $M_{\text{BH}}-\sigma_*$ slope becomes slightly negative since the NLS1s are mainly located at the low M_{BH} and low stellar velocity dispersion region. Considering the small offset and the limited mass distribution, NLS1s seem to show a consistent $M_{\text{BH}}-\sigma_*$ relation compared to the RM AGNs.

Among NLS1s, there is a large scatter with a clear trend with the host galaxy morphology. Compared to the best-fit $M_{\text{BH}}-\sigma_*$ relation of the joint sample of quiescent galaxies and RM AGNs, early-type NLS1s show a positive offset ($\Delta \log M_{\text{BH}} = 0.32 \pm 0.10$ and $\Delta \log M_{\text{BH}} = 0.20 \pm 0.10$, respectively in the left and right panels) while late-type galaxies present a negative offset ($\Delta \log M_{\text{BH}} = -0.13 \pm 0.06$ and $\Delta \log M_{\text{BH}} = -0.25 \pm 0.06$, respectively in the left and right panels in Figure 4). The large difference of the offset between early-type and late-type NLS1 galaxies may stem from the effect of the rotational broadening in the stellar absorption lines since single aperture spectra have been used for measuring the stellar velocity dispersion. To test this scenario, we further divide the late-type NLS1 galaxies into two groups, i.e., edge-on and face-on galaxies (see Section 3.4 for morphology classification), and calculated the mean offset. Clearly, the edge-on late type galaxies, which are expected to have larger rotational broadening in the line-of-sight stellar velocity dispersion measurements, show the largest negative offset ($\Delta \log M_{\text{BH}} = -0.47 \pm 0.15$ and $\Delta \log M_{\text{BH}} = -0.64 \pm 0.15$, respectively in the left and right panels in Figure 4), while the face-on galaxies do not show a clear offset ($\Delta \log M_{\text{BH}} = -0.05 \pm 0.06$ and $\Delta \log M_{\text{BH}} = -0.17 \pm 0.06$, respectively in the left and right panels in Figure 4). Thus, we suspect that the large scatter of the NLS1s in the $M_{\text{BH}}-\sigma_*$ plane and the systematic trend of the offset with galaxy morphology and inclination are due to the rotational broadening (Xiao et al. 2011; Harris et al. 2012; Kang et al. 2013; Woo et al. 2013; Bellovary et al. 2014).

4.2. offset from the $M_{\text{BH}}-\sigma_*$ relation

In this section, we investigate whether the offset from the $M_{\text{BH}}-\sigma_*$ relation is correlated with other AGN parameters, i.e., Eddington ratio, R5007 and R4570. Note that the offset is calculated with respect to the best-fit $M_{\text{BH}}-\sigma_*$ relation of the joint sample of quiescent galaxies and RM AGNs. First, we compare the offset with Eddington ratio in Figure 7

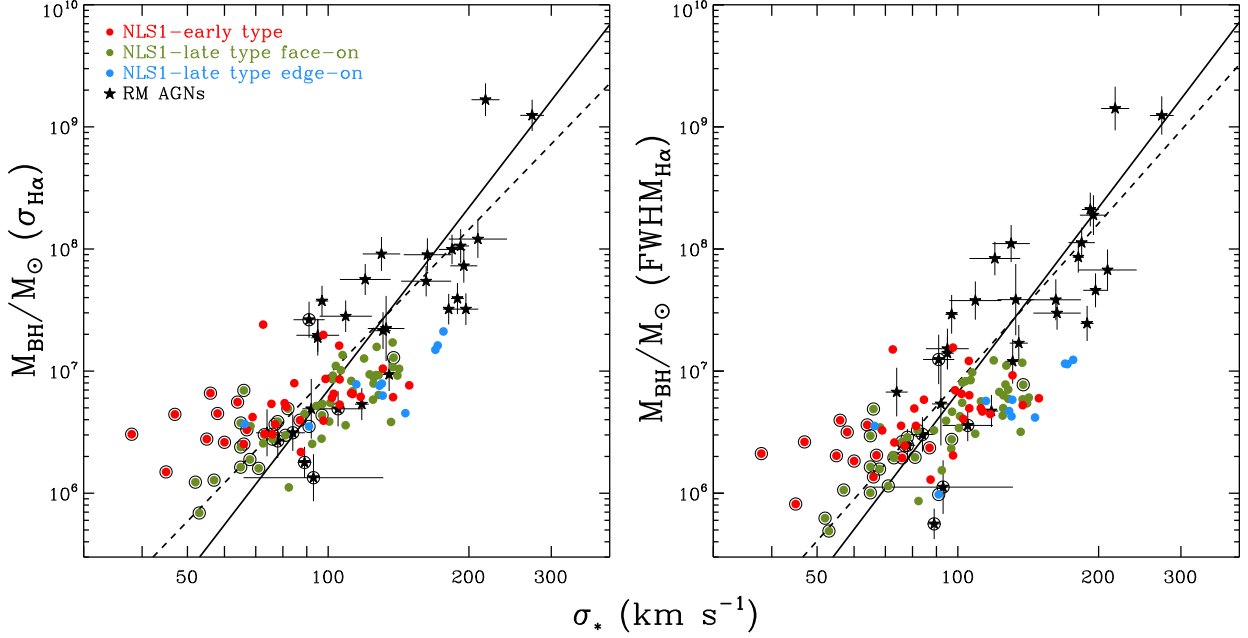


FIG. 6.— $M_{\text{BH}}-\sigma_*$ relations of 93 NLS1s with M_{BH} estimated with $\sigma_{\text{H}\alpha}$ (left) and $\text{FWHM}_{\text{H}\alpha}$ (right), respectively. The morphology and inclination of each galaxy is represented by different colors: early-type (red), more face-on late-type (green), and more edge-on late-type galaxies (blue). The solid line represents the best-fit $M_{\text{BH}}-\sigma_*$ relation of the joint sample of reverberation-mapped AGNs and quiescent galaxies, while the dotted line represents the best-fit $M_{\text{BH}}-\sigma_*$ relation of the reverberation-mapped AGNs only (see Appendix). Six NLS1s among the reverberation-mapped AGNs are denoted with encircled stars. The σ_* values adopted from Xiao et al. (2011) are represented by encircled filled circles.

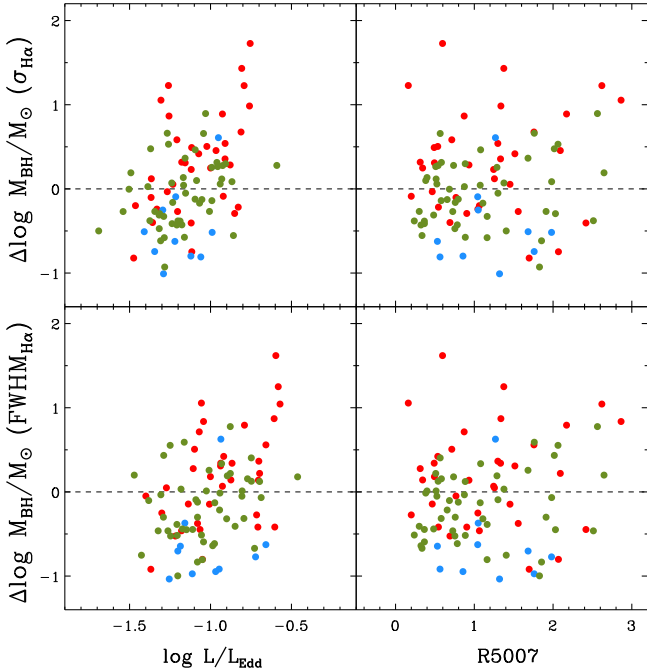


FIG. 7.— Correlations of the offset from the $M_{\text{BH}}-\sigma_*$ relation with L/L_{Edd} and R5007. The colors express same as in Figure 6.

(left), finding no significant correlation between the offset and L/L_{Edd} (see consistent results by Komossa & Xu 2007). For this comparison, Eddington ratio was determined by dividing the bolometric luminosity by the Eddington luminosity, $L_{\text{Edd}} = 1.26 \times 10^{38} \times M_{\text{BH}}$, using the continuum luminosity at 5100\AA as a proxy ($L_{\text{bol}} = 9\lambda L_{5100}$) (Kaspi et al. 2000; Peterson et al. 2004). We also used the $\text{H}\alpha$ line luminosity

instead of the continuum luminosity at 5100\AA based on Equation 4, and obtained the same results. Second, we present the comparison between the offset and R5007 in Figure 7. R5007 does not significantly correlate with the offset of NLS1s in general and in all three different morphology groups.

In Figure 8, we compare the Fe II strength (R4570) with the offset from the $M_{\text{BH}}-\sigma_*$ relation. There is a weak correlation between them: while the weak Fe II emitters show both positive and negative offsets, the strong Fe II emitters mainly show negative offset (see the reference line at R4570 = 1; Lawrence et al. 1988; Zhou et al. 2006). This result implies that NLS1s with strong Fe II more significantly deviate from the $M_{\text{BH}}-\sigma_*$ relation. The correlation is slightly different for different morphology groups. However, the sample size in each morphology group is too small to definitely claim any difference.

In addition, we tested whether the offset from the $M_{\text{BH}}-\sigma_*$ relation is related with the AGN fraction (see Figure 8 right panels), using the AGN fraction determined from the monochromatic flux ratio of AGN to host galaxy at 5100\AA . We find a good correlation of the offset with the AGN fraction: the offset positively increases with increasing AGN fraction. This correlation is also present in each morphology group while early-type galaxies have on average higher AGN fraction than late type galaxies. The interpretation of this correlation is not straightforward since a strong selection effect is involved in measuring stellar velocity dispersion. For example, if the AGN fraction is higher, then it is more difficult to measure stellar velocity dispersion. Hence, only massive early-type galaxies are available at high AGN fraction regime, while most late-type galaxies hosting high luminosity AGNs are missing from the distribution.

5. DISCUSSION

5.1. The effect of rotational broadening

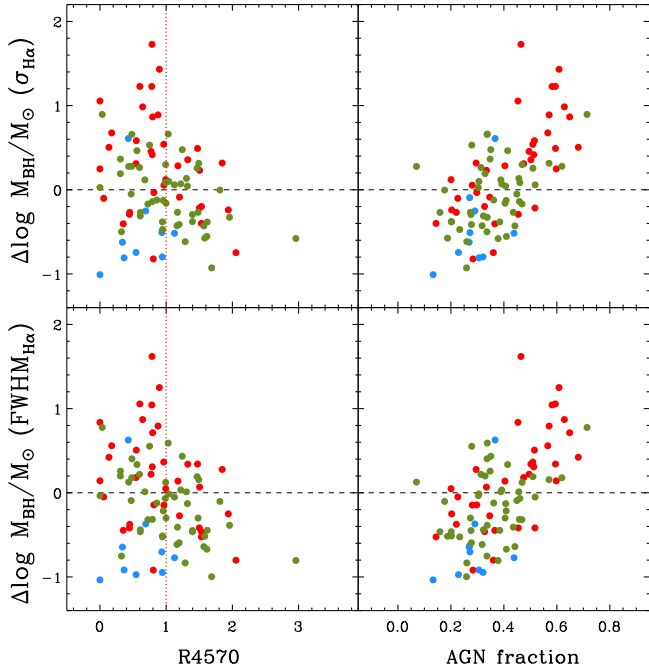


FIG. 8.— Left: comparison of the offset from the AGN $M_{\text{BH}} - \sigma_*$ relation with R4570 (left) and AGN fraction (right). The colors express same as in Figure 6.

The contribution of the rotation of stellar disks can bias stellar velocity dispersion measurements due to the rotational broadening of the stellar absorption lines. For example, if a single-aperture spectrum, which is integrated over a large portion of a stellar disk, is used for measuring the second moment of the absorption lines, the rotational effect can significantly increase the velocity dispersion measurements. For early-type galaxies the rotation effect is relatively small since the velocity dispersion is typically higher than rotation velocity. For example, Kang et al. (2013) reported that the stellar velocity dispersion changes by $\sim 10\%$ as a function of the aperture size, based on the spatially resolved measurements of 31 early-type galaxies in the $M_{\text{BH}} - \sigma_*$ sample. In contrast, we expect the rotation effect can be substantially larger in late-type galaxies than in early-type galaxies due to much higher velocity-to-dispersion (V/σ) ratios. For disk-dominant late-type galaxies, the inclination to the line-of-sight can also play a significant role due to the project effect. Based on the n-body smoothed particle hydrodynamic simulations, Bellovary et al. (2014) reported that bulge stellar velocity dispersion measurements can change by 30% depending on the galaxy inclination.

Since most of the σ_* measurements for AGN host galaxies are based single-aperture spectra, the effect of rotation and inclination can play a role in comparing BL AGNs with NLS1s. Using a sample of low M_{BH} AGN sample, Xiao et al. (2011) showed a clear dependency of galaxy inclination on the offset from the $M_{\text{BH}} - \sigma_*$ relation, i.e., more inclined galaxies tend to have higher σ_* and negatively offset, while more face-on galaxies tend to have lower σ_* and positively offset. The observed trend of the offset from the $M_{\text{BH}} - \sigma_*$ relation with galaxy inclination in our study is similar to Xiao et al. (2011), reflecting the same effect of the rotation and inclination of late-type galaxies. Thus, the conclusion that NLS1s follow the same $M_{\text{BH}} - \sigma_*$ relation as BL AGNs is still limited by the lack of spatially resolved measurements. To better understand

the effect of rotation and inclination, spatially resolved measurements are required for NLS1s, which is beyond the scope of the current study.

5.2. NLS1s versus BL AGNs

Two different scenarios have been suggested for the evolution of NLS1s. On the one hand, NLS1s are considered as the precursors of BL AGNs, evolving into BL AGNs. The low M_{BH} and the high Eddington ratio of NLS1s may imply that NLS1s are young phase of AGNs (Véron-Cetty et al. 2001; Mathur et al. 2001; Boroson 2002). On the other hand, NLS1s are viewed as an extension of BL AGNs at the low-mass scale (McHardy et al. 2006). If the high Eddington ratio of NLS1s represents a relatively short-lived accretion phase, and the Eddington ratio before and after the strong accretion phase is relatively low, then the black hole growth in NLS1 may be insignificant. We find no significant evidence that NLS1 offset from the $M_{\text{BH}} - \sigma_*$ relation of active and inactive galaxies, suggesting that NLS1s and BL AGNs are similar in terms of the current black hole growth. In the case of the host galaxies of NLS1s, there seems no strong difference between the environments of NLS1s and BL AGNs (Krongold et al. 2001). Also, NLS1s are not preferentially hosted by merging galaxies (Ryan et al. 2007). Thus, the growth of black holes and host galaxies seem to be similar between NLS1 and BL AGNs.

Based on the estimates of the bolometric luminosity of the NLS1s in our sample, we calculated the mass accretion rate in order to investigate the black hole growth time scale. For given the range of bolometric luminosity of $10^{43} - 10^{44} \text{ erg s}^{-1}$, we estimate the mass accretion rate as $\sim 0.002 - \sim 0.02 M_{\odot} \text{ year}^{-1}$. Thus, in order to accrete a million solar mass to a black hole with a constant mass accretion rate of $\sim 0.002 - \sim 0.02 M_{\odot} \text{ year}^{-1}$, it would take $10^8 - 10^9 \text{ yrs}$. The mean Eddington ratio of the NLS1s in our sample is $\sim 10\%$, for which the e-folding growth time scale is $4 \times 10^8 \text{ yrs}$. Thus, unless the life time of the AGN activity is comparable to this growth time scale, NLS1s are not expected to move up to the larger M_{BH} direction in the $M_{\text{BH}} - \sigma_*$ plane (see also discussion by Komossa & Xu 2007).

5.3. Inclination angle

NLS1s are often considered as more inclined (pole-on) systems to the line-of-sight than BL AGNs, implying that the measured line-of-sight velocity dispersion (line width) of broad emission lines is relatively narrow due to the projection effect. If this is the case, then the M_{BH} of NLS1s are significantly underestimated and their Eddington ratios are accordingly overestimated. However, although there are some evidences that NLS1s are close to pole-on systems (e.g., Fischer et al. 2014; Foschini et al. 2014), the inclination effect cannot explain the entire NLS1 population (see discussion by Peterson 2011). The implication of the potential inclination effect is that the NLS1s in our sample would positively offset toward the high M_{BH} direction, if the black hole masses were estimated after correcting for the velocity projection effect. In this scenario, it is difficult to understand why NLS1s have higher black hole to galaxy mass ratios compared to BL AGNs and quiescent galaxies.

We note that 6 NLS1s are included in the sample of the reverberation-mapped AGNs, which are used for deriving the average virial factor for type 1 AGNs (see Figure 5). The location of the NLS1s in the $M_{\text{BH}} - \sigma_*$ plane is not different

from that of BL AGNs, implying that the virial factor and inclination angle of the NLS1s may not be very different from those of BL AGNs, although the number of NLS1s in the reverberation-mapped AGN sample is still small to make a firm conclusion.

6. SUMMARY & CONCLUSION

We investigated the $M_{\text{BH}} - \sigma_*$ relation of the present-day NLS1, using directly measured stellar velocity dispersions for a sample of 93 NLS1s at $z < 0.1$ selected from the SDSS. We summarize the main results.

- Compared to the $M_{\text{BH}} - \sigma_*$ relation derived from the joint sample of the reverberation-mapped AGNs and inactive galaxies, the NLS1s in our sample show no significant offset, suggesting that NLS1s are an extension of BL AGNs at lower mass scale.
- Among NLS1s, there is a systematic trend with galaxy

inclination, i.e., more inclined galaxies have larger σ_* at fixed M_{BH} , probably due to the contribution of the rotational broadening in the stellar absorption lines.

- By jointly fitting the $M_{\text{BH}} - \sigma_*$ relation using the most updated reverberation-mapped AGNs and quiescent galaxies, we obtained the virial factor $\log f = 0.65 \pm 0.12$ (i.e., $f = 4.47$) and $\log f = 0.05 \pm 0.12$ (i.e., $f = 1.12$), respectively for M_{BH} estimators based on the $\sigma_{\text{H}\beta}$ and $\text{FWHM}_{\text{H}\beta}$.

We thank the anonymous referee for valuable comments, which improved the clarity of the manuscript. This work was supported by the National Research Foundation of Korea (NRF) grant funded by the Korea government (MEST; No. 2012-006087). J.H.W acknowledges the support by the Korea Astronomy and Space Science Institute (KASI) grant funded by the Korea government (MEST).

APPENDIX

A1. THE VIRIAL FACTOR

The virial factor f in Equation (1) is difficult to determine for individual objects due to the unknown geometry and distribution of the BLR gas (c.f., Brewer et al. 2011; Pancoast et al. 2012, 2014). Instead, an average f has been determined by scaling the reverberation-mapped AGNs to quiescent galaxies in the $M_{\text{BH}} - \sigma_*$ plane, assuming that AGN and non-AGN galaxies follow the same $M_{\text{BH}} - \sigma_*$ relation (Onken et al. 2004; Woo et al. 2010; Woo et al. 2013; Park et al. 2012). While most of these calibrations have been performed using the virial product ($V^2 \times R_{\text{BLR}}/G$) based on $\sigma_{\text{H}\beta}$ as the velocity proxy of the broad-line gas, a number of black hole mass studies used $\text{FWHM}_{\text{H}\beta}$ for estimating single-epoch M_{BH} because of the difficulty of measuring $\sigma_{\text{H}\beta}$ due to the low S/N of available spectra (e.g., SDSS). In this case, $\text{FWHM}_{\text{H}\beta}$ is converted to $\sigma_{\text{H}\beta}$ with a constant FWHM/σ ratio. However, the FWHM/σ ratio has a wide range since the line profile of the $\text{H}\beta$ line is not universal (Peterson et al. 2004; Collin et al. 2006), hence, a systematic uncertainty is added to the mass estimates. Here we provide the f factor for $\sigma_{\text{H}\beta}$ -based and $\text{FWHM}_{\text{H}\beta}$ -based virial products, respectively, by fitting the $M_{\text{BH}} - \sigma_*$ relation.

For the reverberation-mapped AGNs, we collected and updated the time-lag (e.g., Zu et al. 2011), $\text{FWHM}_{\text{H}\beta}$ and $\sigma_{\text{H}\beta}$ as well as stellar velocity dispersion measurements from the literature for a sample of 29 AGNs, as listed in Table A1 (see a recent compilation by Woo et al. 2013 and the addition of Grier et al. 2013 and Bentz et al. 2014), after excluding two objects, PG 1229+204 and PG 1617+175 since their stellar velocity dispersion measurements are very uncertain (see for example Figure 3 in Grier et al. 2013). The $\text{FWHM}_{\text{H}\beta}$ and $\sigma_{\text{H}\beta}$ are measured from the rms spectra of each object except for the 4th entry of Mrk 817 (see Table A1). When there are multiple measurements available for given objects, we calculated the mean of the virial products. Note that we often found typos of the quoted values of the time lag and the $\text{H}\beta$ velocity in the literature. Thus, we included the reference of the original measurements.

In the case of the quiescent galaxy sample, we used 84 galaxies from the compilation of Kormendy & Ho (2013), after excluding 3 galaxies, NGC 2778, NGC 3945, NGC 4382 due to the lack of the lower limit of the black hole mass. Note that the choice of the quiescent galaxy sample does not significantly change the results presented for the NLS1s since the virial factor is determined based on the best-fit $M_{\text{BH}} - \sigma_*$ relation and the M_{BH} of the NLS1s scales accordingly. A careful comparison of the $M_{\text{BH}} - \sigma_*$ relation based on various subsamples of the quiescent galaxies will be presented by Woo et al. (in preparation).

We performed a joint-fit analysis for the combined sample of reverberation-mapped AGNs and quiescent galaxies in order to determine the slope, intercept, and the virial factor, following the joint-fit method as described in Woo et al. 2013:

$$\chi^2 = \sum_{i=1}^N \frac{(\mu_i - \alpha - \beta s_i)^2}{\sigma_{\mu,i}^2 + \beta^2 \sigma_{s,i}^2 + \epsilon_0^2} + \sum_{j=1}^M \frac{(\mu_{\text{VP},j} + \log f - \alpha - \beta s_j)^2}{\sigma_{\mu_{\text{VP},j}}^2 + \beta^2 \sigma_{s,j}^2 + \epsilon_0^2}, \quad (\text{A1})$$

where $\mu = \log(M_{\text{BH}}/M_{\odot})$ of quiescent galaxies, $\mu_{\text{VP}} = \log(V^2 R_{\text{BLR}}/G)$ of reverberation-mapped AGNs, and $s = \log(\sigma_*/200 \text{ km s}^{-1})$, while σ_{μ} , $\sigma_{\mu_{\text{VP}}}$, and σ_s are the measurements uncertainties in μ , μ_{VP} , and s , respectively, and ϵ_0 is intrinsic scatter, which we change for the reduced χ^2 to be unity. In Figure A1, we present the best-fit $M_{\text{BH}} - \sigma_*$ relation for the combined sample. When $\sigma_{\text{H}\beta}$ is used as V in Eq. 1, we obtained the intercept $\alpha = 8.34 \pm 0.05$, the slope $\beta = 4.97 \pm 0.28$, and $\log f = 0.65 \pm 0.12$. In the case of $\text{FWHM}_{\text{H}\beta}$, we derived $\alpha = 8.34 \pm 0.05$, $\beta = 5.04 \pm 0.28$, and $\log f = 0.05 \pm 0.12$. The intrinsic scatter of the combined sample is 0.43 ± 0.03 and 0.43 ± 0.03 , respectively for $\sigma_{\text{H}\beta}$ -based mass and $\text{FWHM}_{\text{H}\beta}$ -based mass. The derived f factor and the $M_{\text{BH}} - \sigma_*$ relation based on the updates of the reverberation and stellar velocity dispersion measurements are consistent with those derived by Woo et al. (2013). In the case of the $\text{FWHM}_{\text{H}\beta}$ -based M_{BH} , the best-fit virial factor $f = 1.12$ is consistent with the value derived by Collin et al. (2006). For future M_{BH} studies, we recommend to use $\log f = 0.65 \pm 0.12$ for the $\sigma_{\text{H}\beta}$ -based M_{BH} estimates, and $\log f = 0.05 \pm 0.12$ for the $\text{FWHM}_{\text{H}\beta}$ -based M_{BH} estimates. The derived virial factor is consistent with that determined from the dynamical modeling based on the velocity-resolved measurements of five AGNs (Pancoast et al. 2014), which are $\log f = 0.68 \pm 0.40$ and $\log f = -0.07 \pm 0.40$, respectively for the $\sigma_{\text{H}\beta}$ -based and $\text{FWHM}_{\text{H}\beta}$ -based black hole masses.

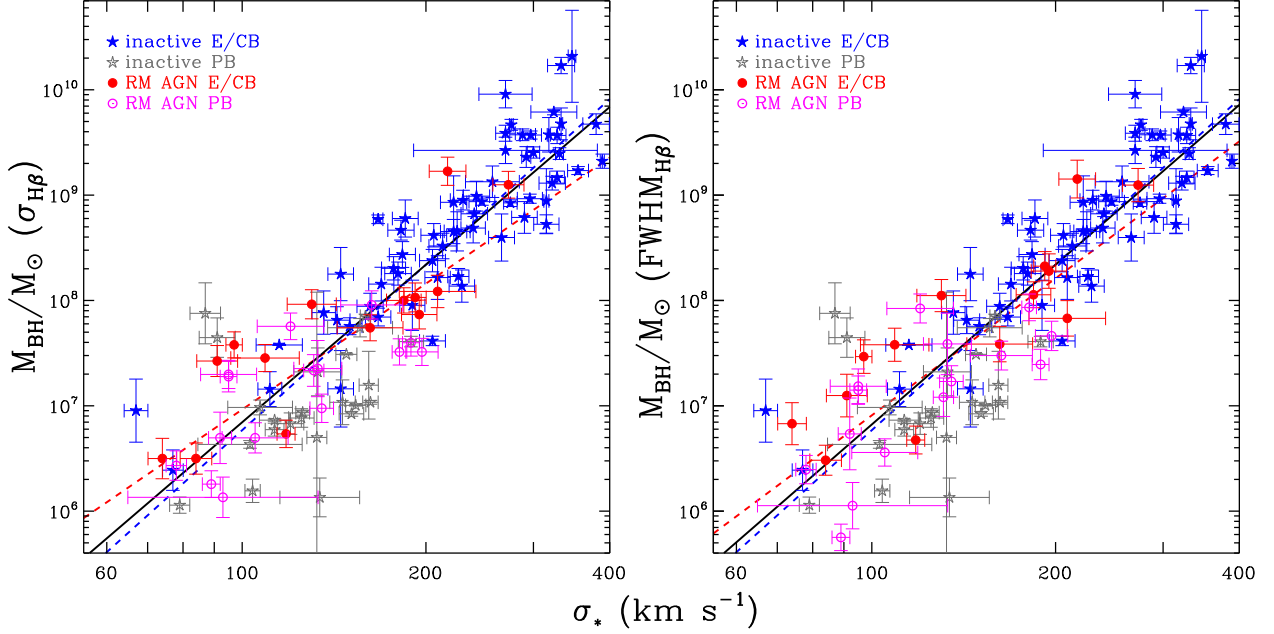


FIG. 9.— $M_{\text{BH}} - \sigma_*$ relation of quiescent (blue and grey stars) and active (red and magenta circles) galaxies with AGN M_{BH} estimated from $\sigma_{\text{H}\beta}$ (left) and $\text{FWHM}_{\text{H}\beta}$ (right), respectively. Based on the joint fit result, we used $\log f = 0.65 \pm 0.12$ for the $\sigma_{\text{H}\beta}$ -based M_{BH} and $\log f = 0.05 \pm 0.12$ for the $\text{FWHM}_{\text{H}\beta}$ -based M_{BH} . The solid line represents the best fit for the combined sample of quiescent galaxies and the reverberation-mapped AGNs while the red dashed line represents the best-fit for the reverberation-mapped AGN only. We also present the best-fit $M_{\text{BH}} - \sigma_*$ relation for the quiescent galaxy sample only (blue dashed line), which is consistent with the best fit of the joint sample. This is due to the fact that the quiescent galaxy sample has a similar dynamical range compared to the combined sample. Pseudo-bulge galaxies are denoted with open symbols (magenta circles for active galaxies; grey stars for quiescent galaxies) while ellipticals and pseudo-bulges are represented by filled symbols.

Note that we did not attempt to use a different $M_{\text{BH}} - \sigma_*$ relation for pseudo-bulge galaxies since the $M_{\text{BH}} - \sigma_*$ relation of the pseudo-bulge galaxies is not well defined due to the limited dynamical range (see Figure A1). It is not clear whether pseudo-bulge galaxies offset from the $M_{\text{BH}} - \sigma_*$ relation of classical bulges in Figure A1 (see also Bennert et al. 2014). More detailed comparison of pseudo-bulge galaxies in the $M_{\text{BH}} - \sigma_*$ plane will be provided by Woo et al. (in preparation) based on the new measurements from the spatially-resolved kinematics of 9 pseudo-bulge galaxies. Thus, in this study we simply combine classical and pseudo bulges in determining the best fit $M_{\text{BH}} - \sigma_*$ relation. In Figure A1, we used open symbols for pseudo bulge galaxies following the classification from Kormendy & Ho 2014 and Ho & Kim 2014.

As a consistency check, we fit the $M_{\text{BH}} - \sigma_*$ relation for the AGN sample only by minimizing

$$\chi^2 = \sum_{i=1}^N \frac{(\mu_i - \alpha - \beta s_i)^2}{\sigma_{\mu,i}^2 + \beta^2 \sigma_{s,i}^2 + \epsilon_0^2}, \quad (\text{A2})$$

where we used $\log f = 0.65$ for the $\sigma_{\text{H}\beta}$ -based M_{BH} estimates, and $\log f = 0.05$ for $\text{FWHM}_{\text{H}\beta}$ -based M_{BH} . Using the $\sigma_{\text{H}\beta}$ -based M_{BH} , we obtained the best-fit $\alpha = 8.16 \pm 0.18$, $\beta = 3.97 \pm 0.56$, and the intrinsic scatter $\epsilon = 0.41 \pm 0.05$. In the case of the $\text{FWHM}_{\text{H}\beta}$ -based M_{BH} , we derived $\alpha = 8.21 \pm 0.18$, $\beta = 4.32 \pm 0.59$, and $\epsilon = 0.43 \pm 0.05$. These slopes are consistent with the best-fit slope of the combined sample within the uncertainties. We note that the slope α of the AGN $M_{\text{BH}} - \sigma_*$ relation does not depend on the choice of the virial factor in Equation A2.

We emphasize that in our study the $M_{\text{BH}} - \sigma_*$ relation of the reverberation-mapped AGNs is derived with a consistent method adopted for the quiescent galaxies (see Park et al. 2012), while other studies of AGN $M_{\text{BH}} - \sigma_*$ relation often utilized somewhat different method, without including an iterative fitting process with intrinsic scatter. Compared to Grier et al. (2013), for example, we obtained a different $M_{\text{BH}} - \sigma_*$ relation, hence, the virial factor even if we used the compiled values in their table. This discrepancy seems to stem from the treatment of the intrinsic scatter since we obtained the same results as Grier et al. (2013) when we excluded the intrinsic scatter in the fitting process.

TABLE 2
VIRIAL PRODUCTS AND σ_* OF THE REVERBERATION-MAPPED AGNS

Name	$\tau_{H\beta}$ (days)	Ref.	σ_{line} (km s $^{-1}$)	FWHM $_{H\beta}$ (km s $^{-1}$)	Ref.	VP(σ_{line}) (10 6 M $_{\odot}$)	VP(FWHM $_{H\beta}$) (10 6 M $_{\odot}$)	σ_* (km s $^{-1}$)	Ref.
(1)	(2)	(3)	(4)	(5)	(6)	(7)	(8)	(9)	(10)
3C 120	27.2 $^{+1.1}_{-1.1}$	1	1514 \pm 65	2539 \pm 466	1	12.2 $^{0.9}_{-0.9}$	34.2 $^{9.0}_{-9.0}$	162 \pm 20	13
3C 390.3	47.9 $^{+2.4}_{-4.7}$	2	5455 \pm 278	10872 \pm 1670	2	278.1 $^{24.4}_{-31.6}$	1104.8 $^{246.3}_{-258.8}$	273 \pm 16	14
Ark 120	35.7 $^{+9.7}_{-9.2}$	3	1959 \pm 109	5536 \pm 297	4	26.7 $^{5.4}_{-7.2}$	213.5 $^{43.2}_{-37.4}$		
	29.7 $^{+3.3}_{-5.9}$	3	1884 \pm 48	5284 \pm 203	4	20.6 $^{2.4}_{-4.2}$	161.8 $^{20.0}_{-33.3}$	192 \pm 8	15
mean						23.7 $^{3.0}_{-4.2}$	187.7 $^{23.8}_{-33.2}$		
Arp 151	3.6 $^{+0.7}_{-0.2}$	5	1295 \pm 37	2458 \pm 82	6	1.2 $^{0.2}_{-0.1}$	4.2 $^{0.8}_{-0.3}$	118 \pm 4	16
Mrk 50	10.6 $^{+0.3}_{-0.9}$	7	1740 \pm 101	4039 \pm 606 ^a	7	6.3 $^{0.1}_{-0.7}$	33.7 $^{7.6}_{-7.7}$	109 \pm 14	7
Mrk 79	25.5 $^{+2.9}_{-14.4}$	3	2137 \pm 375	5086 \pm 1436	4	22.7 $^{6.2}_{-14.0}$	128.7 $^{53.4}_{-89.0}$		
	30.9 $^{+1.4}_{-2.1}$	3	1683 \pm 72	4219 \pm 262	4	17.1 $^{1.3}_{-1.3}$	107.3 $^{10.6}_{-11.9}$		
	17.2 $^{+7.3}_{-2.2}$	3	1854 \pm 72	5251 \pm 533	4	11.5 $^{4.9}_{-1.6}$	92.5 $^{41.1}_{-17.8}$		
	43.6 $^{+1.7}_{-0.8}$	3	1883 \pm 246	2786 \pm 390	4	30.2 $^{5.7}_{-5.6}$	66.0 $^{13.3}_{-13.1}$	130 \pm 12	14
mean						20.4 $^{2.5}_{-3.8}$	98.7 $^{17.4}_{-23.1}$		
Mrk 110	25.3 $^{+2.3}_{-13.1}$	3	1196 \pm 141	1494 \pm 802	4	7.1 $^{1.3}_{-3.8}$	11.0 $^{8.4}_{-10.1}$		
	33.9 $^{+6.1}_{-5.3}$	3	1115 \pm 103	1381 \pm 528	4	8.2 $^{1.8}_{-1.7}$	12.6 $^{7.2}_{-7.1}$		
	21.5 $^{+2.2}_{-2.1}$	3	755 \pm 29	1521 \pm 59	4	2.4 $^{0.3}_{-0.3}$	9.7 $^{1.1}_{-1.1}$	91 \pm 7	17
mean						5.9 $^{0.8}_{-1.4}$	11.1 $^{3.7}_{-4.1}$		
Mrk 202	3.5 $^{+0.1}_{-0.1}$	5	962 \pm 67	1794 \pm 181	6	0.6 $^{0.1}_{-0.1}$	2.2 $^{0.3}_{-0.3}$	78 \pm 3	16
Mrk 279	18.3 $^{+1.2}_{-1.1}$	3	1420 \pm 96	3385 \pm 349	4	7.2 $^{0.8}_{-0.8}$	40.9 $^{6.5}_{-6.5}$	197 \pm 12	14
Mrk 509	69.9 $^{+0.3}_{-1.8}$	3	1276 \pm 28	2715 \pm 101	4	22.2 $^{0.7}_{-0.7}$	100.5 $^{5.2}_{-5.3}$	184 \pm 12	5
Mrk 590	19.0 $^{+1.8}_{-2.6}$	3	789 \pm 74	1675 \pm 587	4	2.3 $^{0.4}_{-0.4}$	10.4 $^{5.2}_{-5.3}$		
	19.5 $^{+2.0}_{-4.0}$	3	1935 \pm 52	2566 \pm 106	4	14.2 $^{1.6}_{-3.0}$	25.1 $^{3.0}_{-5.3}$		
	32.6 $^{+3.3}_{-3.3}$	3	1251 \pm 72	2115 \pm 575	4	10.0 $^{1.3}_{-2.8}$	28.5 $^{11.4}_{-13.4}$		
	30.9 $^{+2.5}_{-2.4}$	3	1201 \pm 130	1979 \pm 386	4	8.7 $^{1.5}_{-1.5}$	23.6 $^{6.8}_{-6.8}$	189 \pm 6	14
mean						8.8 $^{0.6}_{-1.1}$	21.9 $^{3.6}_{-4.2}$		
Mrk 817	20.9 $^{+2.3}_{-5.3}$	3	1392 \pm 78	3515 \pm 393	4	7.9 $^{1.1}_{-1.1}$	50.4 $^{9.7}_{-9.7}$		
	17.2 $^{+1.9}_{-2.7}$	3	1971 \pm 96	4952 \pm 537	4	13.0 $^{2.2}_{-2.2}$	82.3 $^{15.6}_{-18.1}$		
	35.9 $^{+4.8}_{-5.8}$	3	1729 \pm 158	3752 \pm 995	4	20.9 $^{3.9}_{-4.3}$	98.6 $^{39.3}_{-40.3}$		
	10.8 $^{+1.5}_{-1.0}$	3	2025 \pm 5 ^b	5627 \pm 30 ^b	8	8.6 $^{1.2}_{-0.8}$	66.7 $^{9.3}_{-6.2}$	120 \pm 15	14
mean						12.6 $^{1.1}_{-1.3}$	74.5 $^{11.1}_{-11.4}$		
Mrk 1310	4.2 $^{+0.9}_{-0.1}$	5	921 \pm 135	1823 \pm 157	6	0.7 $^{0.2}_{-0.1}$	2.7 $^{0.7}_{-0.3}$	84 \pm 5	16
NGC 3227	10.6 $^{+6.1}_{-6.1}$	3	2018 \pm 174	5278 \pm 1117	4	8.4 $^{5.0}_{-5.0}$	57.6 $^{37.4}_{-37.4}$		
	4.4 $^{+0.3}_{-0.5}$	3	1376 \pm 44	3578 \pm 83	8	1.6 $^{0.1}_{-0.2}$	11.0 $^{0.8}_{-1.3}$	133 \pm 12	18
mean						5.0 $^{2.5}_{-2.5}$	34.3 $^{18.7}_{-18.7}$		
NGC 3516	14.6 $^{+1.4}_{-1.1}$	3	1591 \pm 10	5175 \pm 96	8	7.2 $^{0.7}_{-0.5}$	76.3 $^{7.6}_{-6.1}$	181 \pm 5	14
NGC 3783	7.3 $^{+0.3}_{-0.7}$	3	1753 \pm 141	3093 \pm 529	4	4.4 $^{0.5}_{-0.7}$	13.6 $^{3.3}_{-3.5}$	95 \pm 10	19
NGC 4051	2.5 $^{+0.1}_{-0.1}$	3	927 \pm 64	1034 \pm 41	8	0.4 $^{0.04}_{-0.04}$	0.5 $^{0.04}_{-0.04}$	89 \pm 3	14
NGC 4151	6.0 $^{+0.6}_{-0.2}$	3	2680 \pm 64	4711 \pm 750	9	8.4 $^{0.9}_{-0.4}$	26.0 $^{6.4}_{-5.9}$	97 \pm 3	14
NGC 4253	5.4 $^{+0.2}_{-0.8}$	5	538 \pm 82	986 \pm 251	6	0.3 $^{0.1}_{-0.1}$	1.0 $^{0.4}_{-0.4}$	93 \pm 32	16
NGC 4593	4.5 $^{+0.7}_{-0.6}$	3	1561 \pm 55	4141 \pm 416	10	2.1 $^{0.3}_{-0.3}$	15.1 $^{3.2}_{-2.9}$	135 \pm 6	14
NGC 4748	8.6 $^{+0.6}_{-0.4}$	5	791 \pm 80	1373 \pm 86	6	1.1 $^{0.2}_{-0.2}$	3.2 $^{0.4}_{-0.3}$	105 \pm 13	16
NGC 5273	1.4 $^{+1.1}_{-0.1}$	11	1544 \pm 98	4615 \pm 330	11	0.7 $^{0.5}_{-0.1}$	6.0 $^{4.6}_{-0.9}$	74 \pm 4	20
NGC 5548	5.5 $^{+0.6}_{-0.7}$	5	3900 \pm 266	12539 \pm 1927	6	16.3 $^{2.4}_{-2.6}$	168.7 $^{71.0}_{-42.5}$	195 \pm 13	16
NGC 6814	7.4 $^{+0.1}_{-0.5}$	5	1697 \pm 224	2945 \pm 283	6	4.2 $^{0.8}_{-0.8}$	12.5 $^{1.7}_{-1.7}$	95 \pm 3	16
NGC 7469	11.7 $^{+0.5}_{-0.7}$	3	1456 \pm 207	2169 \pm 459	4	4.8 $^{1.0}_{-1.0}$	10.7 $^{3.2}_{-3.3}$	131 \pm 5	14
PG 1411+442	53.5 $^{+13.1}_{-5.3}$	3	1607 \pm 169	2398 \pm 353	4	27.0 $^{7.0}_{-4.8}$	60.0 $^{19.3}_{-13.8}$	209 \pm 30	5
PG 1426+015	161.6 $^{+6.9}_{-11.1}$	3	3442 \pm 308	6323 \pm 1295	4	373.6 $^{49.9}_{-53.8}$	1260.8 $^{369.1}_{-375.3}$	217 \pm 15	21
PG 2130+099	31.0 $^{+4.0}_{-4.0}$	12	1825 \pm 65	2097 \pm 102	1	20.1 $^{2.8}_{-2.8}$	26.6 $^{3.9}_{-3.9}$	163 \pm 19	5
SBS 1116+583A	2.4 $^{+0.9}_{-0.9}$	5	1550 \pm 310	3202 \pm 1127	6	1.1 $^{0.5}_{-0.5}$	4.8 $^{3.0}_{-3.0}$	92 \pm 4	16

Ref. — (1) Grier et al. 2012; (2) Dietrich et al. 2012; (3) Zu et al. 2011; (4) Peterson et al. 2004; (5) Grier et al. 2013b; (6) Park et al. 2012; (7) Barth et al. 2011; (8) Denney et al. 2010; (9) Bentz et al. 2006; (10) Denney et al. 2006; (11) Bentz et al. 2014; (12) Grier et al. 2013a; (13) Nelson & Whittle 1995; (14) Nelson et al. 2004; (15) Woo et al. 2013; (16) Woo et al. 2010; (17) Ferrarese et al. 2001; (18) Kormendy & Ho 2013; (19) Onken et al. 2004; (20) Cappellari et al. 2013; (21) Watson et al. 2008

Notes.

^a FWHM $_{H\beta}$ is measured from the rms spectrum in Barth et al. 2011.

^b Only for this entry, FWHM $_{H\beta}$ and $\sigma_{H\beta}$ are measured from the mean spectrum (Denney et al. 2010). All line width measurements except for this entry are measured from rms spectra.

REFERENCES

- Abdo, A. A., Ackermann, M., Ajello, M., et al. 2009, *ApJ*, 707, L142
- Abazajian, K. N., Adelman-McCarthy, J. K., Agüeros, M. A., et al. 2009, *ApJS*, 182, 543
- Antonucci, R. 1993, *ARA&A*, 31, 473
- Bae, H.-J., & Woo, J.-H. 2014, *ApJ*, 795, 30
- Barth, A. J., Ho, L. C., & Sargent, W. L. W. 2002, *ApJ*, 566, L13
- , 2003, *ApJ*, 583, 134
- Barth, A. J., Nguyen, M. L., Malkan, M. A., et al. 2011, *ApJ*, 732, 121
- Barth, A. J., Pancoast, A., Bennert, V. N., et al. 2013, *ApJ*, 769, 128
- Bellovary, J., Holley-Bockelmann, K., Gültekin, K., et al. 2014, arXiv:1405.0286
- Bennert, V. N., Auger, M. W., Treu, T., Woo, J.-H., & Malkan, M. A. 2011, *ApJ*, 726, 59
- Bennert, V. N., Auger, M. W., Treu, T., Woo, J.-H., & Malkan, M. A. 2011, *ApJ*, 742, 107
- Bennert, V. N., Auger, M. W., Treu, T., Woo, J.-H., & Malkan, M. A. 2014, *ApJ*, submitted
- Bentz, M. C., Denney, K. D., Cackett, E. M., et al. 2006, *ApJ*, 651, 775
- Bentz, M. C., Peterson, B. M., Netzer, H., Pogge, R. W., & Vestergaard, M. 2009a, *ApJ*, 697, 160
- , 2009b, *ApJ*, 697, 160
- Bentz, M. C., Denney, K. D., Grier, C. J., et al. 2013, *ApJ*, 767, 149
- Bian, W., Yuan, Q., & Zhao, Y. 2006, *MNRAS*, 367, 860
- Booth, C. M., & Schaye, J. 2011, *MNRAS*, 413, 1158
- Boroson, T. A. 2002, *ApJ*, 565, 78
- Boroson, T. 2005, *AJ*, 130, 381
- Boroson, T. A., & Green, R. F. 1992, *ApJS*, 80, 109
- Botte, V., Ciroi, S., Rafanelli, P., & Di Mille, F. 2004, *AJ*, 127, 3168
- Bower, R. G., Benson, A. J., Malbon, R., et al. 2006, *MNRAS*, 370, 645
- Brewer, B. J., et al. 2011, *ApJ*, 733, L33
- Bruzual, G., & Charlot, S. 2003, *MNRAS*, 344, 1000
- Caccianiga, A., Antón, S., Ballo, L., et al. 2014, *MNRAS*, 441, 172
- Cappellari, M., & Emsellem, E. 2004, Parametric Recovery of Line-of-Sight Velocity Distributions from Absorption-Line Spectra of Galaxies via Penalized Likelihood, *PASP*, 116, 138
- Collin, S., Kawaguchi, T., Peterson, B. M., & Vestergaard, M. 2006, *A&A*, 456, 75
- Crenshaw, D. M., Kraemer, S. B., & Gabel, J. R. 2003, *AJ*, 126, 1690
- Croton, D. J. 2006, *MNRAS*, 369, 1808
- Denney, K. D., Bentz, M. C., Peterson, B. M., et al. 2006, *ApJ*, 653, 152
- Denney, K. D., Peterson, B. M., Pogge, R. W., et al. 2010, *ApJ*, 721, 715
- Dietrich, M., Peterson, B. M., Grier, C. J., et al. 2012, *ApJ*, 757, 53
- Ferrarese, L., & Merritt, D. 2000, *ApJ*, 539, L9
- Ferrarese, L., Pogge, R. W., Peterson, B. M., et al. 2001, *ApJ*, 555, L79
- Fischer, T. C., Crenshaw, D. M., Kraemer, S. B., Schmitt, H. R., & Turner, T. J. 2014, *ApJ*, 785, 25
- Foschini, L., Berton, M., Caccianiga, A., et al. 2014, arXiv:1409.3716
- Gebhardt, K., Bender, R., Bower, G., et al. 2000, *ApJ*, 539, L13
- Goodrich, R. W. 1989, *ApJ*, 342, 224
- Greene, J. E., & Ho, L. C. 2005, *ApJ*, 630, 122
- Greene, J. E., & Ho, L. C. 2006, *ApJ*, 641, 117
- Grier, C. J., Peterson, B. M., Pogge, R. W., et al. 2012, *ApJ*, 755, 60
- Grier, C. J., Peterson, B. M., Horne, K., et al. 2013, *ApJ*, 764, 47
- Grier, C. J., Martini, P., Watson, L. C., et al. 2013, *ApJ*, 773, 90
- Grupe, D. 2004, *AJ*, 127, 1799
- Grupe, D., & Mathur, S. 2004, *ApJ*, 606, L41
- Häring, N., & Rix, H.-W. 2004, *ApJ*, 604, L89
- Harris, C. E., Bennert, V. N., Auger, M. W., et al. 2012, *ApJS*, 201, 29
- Hiner, K. D., Canalizo, G., Wold, M., Brotherton, M. S., & Cales, S. L. 2012, *ApJ*, 756, 162
- Kang, W.-R., Woo, J.-H., Schulze, A., et al. 2013, *ApJ*, 767, 26
- Kaspi, S., Maoz, D., Netzer, H., et al. 2005, *ApJ*, 629, 61
- Kaspi, S., Smith, P. S., Netzer, H., et al. 2000, *ApJ*, 533, 631
- Komossa, S., & Xu, D. 2007, *ApJ*, 667, L33
- Komossa, S., Xu, D., Zhou, H., Storchi-Bergmann, T., & Binette, L. 2008, *ApJ*, 680, 926
- Kormendy, J., & Ho, L. C. 2013, *ARA&A*, 51, 511
- Krongold, Y., Dultzin-Hacyan, D., & Marziani, P. 2001, *AJ*, 121, 702
- Lawrence, A., Saunders, W., Rowan-Robinson, M., et al. 1988, *MNRAS*, 235, 261
- Leighly, K. M. 1999, *ApJS*, 125, 317
- Marconi, A., & Hunt, L. K. 2003, *ApJ*, 589, L21
- Markwardt, C. B. 2009, in *Astronomical Society of the Pacific Conference Series*, Vol. 411, *Astronomical Data Analysis Software and Systems XVIII*, ed. D. A. Bohlender, D. Durand, & P. Dowler, 251
- Mathur, S., & Grupe, D. 2005a, *A&A*, 432, 463
- , 2005b, *ApJ*, 633, 688
- Mathur, S., Kuraszkiewicz, J., & Czerny, B. 2001, *NewA*, 6, 321
- McConnell, N. J., & Ma, C.-P. 2013, *ApJ*, 764, 184
- McGill, K. L., Woo, J.-H., Treu, T., & Malkan, M. A. 2008, *ApJ*, 673, 703
- McHardy, I. M., Koerding, E., Knigge, C., Uttley, P., & Fender, R. P. 2006, *Nature*, 444, 730
- Merritt, D., & Ferrarese, L. 2001, *ApJ*, 547, 140
- Nelson, C. H., & Whittle, M. 1995, *ApJS*, 99, 67
- Nelson, C. H. 2000, *ApJ*, 544, L91
- Nelson, C. H., Green, R. F., Bower, G., Gebhardt, K., & Weistrop, D. 2004, *ApJ*, 615, 652
- Netzer, H., Maoz, D., Laor, A., et al. 1990, *ApJ*, 353, 108
- Ohta, K., Aoki, K., Kawaguchi, T., & Kiuchi, G. 2007, *ApJS*, 169, 1
- Onken, C. A., Ferrarese, L., Merritt, D., et al. 2004, *ApJ*, 615, 645
- Osterbrock, D. E. 1978, *Proceedings of the National Academy of Science*, 75, 540
- Osterbrock, D. E., & Pogge, R. W. 1985, *ApJ*, 297, 166
- Park, D., Woo, J.-H., Treu, T., et al. 2012, *ApJ*, 747, 30
- Park, D., Woo, J.-H., Bennert, V., et al. 2014, *ApJ*, submitted
- Pancoast, A., Brewer, B. J., Treu, T., et al. 2012, *ApJ*, 754, 49
- Peterson, B. M., Ferrarese, L., Gilbert, K. M., et al. 2004, *ApJ*, 613, 682
- Pancoast, A., Brewer, B. J., Treu, T., et al. 2014, *MNRAS*, in press
- Robertson, B., Hernquist, L., Cox, T. J., et al. 2006, *ApJ*, 641, 90
- Ryan, C. J., De Robertis, M. M., Virani, S., Laor, A., & Dawson, P. C. 2007, *ApJ*, 654, 799
- Valdes, F., Gupta, R., Rose, J. A., Singh, H. P., & Bell, D. J. 2004, *ApJS*, 152, 251
- Tremaine, S., Gebhardt, K., Bender, R., et al. 2002, *ApJ*, 574, 740
- Treu, T., Woo, J.-H., Malkan, M. A., & Blandford, R. D. 2007, *ApJ*, 667, 117
- van der Marel, R. P. 1994, *MNRAS*, 270, 271
- Vanden Berk, D. E., Richards, G. T., Bauer, A., et al. 2001, *AJ*, 122, 549
- Véron-Cetty, M.-P., Véron, P., & Gonçalves, A. C. 2001, *A&A*, 372, 730
- Wang, T., & Lu, Y. 2001, *A&A*, 377, 52
- Watson, L. C., Martini, P., Dasyra, K. M., et al. 2008, *ApJ*, 682, L21
- Watson, L. C., Mathur, S., & Grupe, D. 2007, *AJ*, 133, 2435
- Watson, L. C., Martini, P., Dasyra, K. M., et al. 2008, *ApJ*, 682, L21
- Williams, R. J., Pogge, R. W., & Mathur, S. 2002, *AJ*, 124, 3042
- Woo, J.-H., et al. 2014, *JKAS*, 47, 5
- Woo, J.-H., Schulze, A., Park, D., et al. 2013, *ApJ*, 772, 49
- Woo, J.-H., & Urry, C. M. 2002, *ApJ*, 579, 530
- Woo, J.-H., Treu, T., Malkan, M. A., & Blandford, R. D. 2006, *ApJ*, 645, 900
- Woo, J.-H., Urry, C. M., Lira, P., van der Marel, R. P., & Maza, J. 2004, *ApJ*, 617, 903
- Woo, J.-H., Treu, T., Malkan, M. A., & Blandford, R. D. 2006, *ApJ*, 645, 900
- Woo, J.-H., Urry, C. M., van der Marel, R. P., Lira, P., & Maza, J. 2005, *ApJ*, 631, 762
- Woo, J.-H., Treu, T., Malkan, M. A., & Blandford, R. D. 2008, *ApJ*, 681, 925
- Woo, J.-H., Treu, T., Barth, A. J., et al. 2010, *ApJ*, 716, 269
- Xiao, T., Barth, A. J., Greene, J. E., et al. 2011, *ApJ*, 739, 28
- Xu, D., Komossa, S., Zhou, H., et al. 2012, *AJ*, 143, 83
- Zhang, X., Lu, Y., & Yu, Q. 2012, *ApJ*, 761, 5
- Zhou, H., Wang, T., Yuan, W., et al. 2006, *ApJS*, 166, 128
- Zu, Y., Kochanek, C. S., & Peterson, B. M. 2011, *ApJ*, 735, 80